

# Physics-Informed Deep Learning and its Application in Computational Solid and Fluid Mechanics

Alexandros Papados

*University of Maryland, College Park*

*Applied Mathematics, Applied Statistics, Scientific Computing Program*

(Dated: April 26, 2021)

This paper focuses on solving a variety of problems which arise in computational solid and fluid mechanics using *Physics-Informed Deep Learning* (PIDL) techniques. To date, it has been shown that Physics-Informed Neural Networks (PINNs) is an efficient numerical tool which provides solutions to partial differential equations (PDEs), despite the fact that, theoretically, it exhibits limited capability in solving problems with only continuous solutions. Specifically, we will be solving the compressible Euler equations that model gas and fluid dynamics using an original PINNs formulation, *Weighted-Physics-Informed Neural Networks with Domain Extension* (W-PINNs-DE). In addition, we solve a plane stress linear elasticity boundary value problem (LEBVP) from solid mechanics, using a variation of W-PINNs-DE, W-PINNs. In an effort to demonstrate the extent of W-PINNs-DE, we will solve six hydrodynamic shock-tube test problems. Each of these problems yields solutions that develop discontinuities, such as shocks and rarefaction fans. The suite of hydrodynamic problems chosen in this paper are widely used as a validation tool to ensure the ability of newly developed numerical schemes to capture, within tolerable levels, the solutions of the PDEs at hand. Herewith, we validate W-PINNs-DE in the same manner. The proposed solver yields higher accuracy on a class of hydrodynamic shock-tube problems than other PINNs and finite volume methods. Moreover, we validate W-PINNs by solving a LEBVP on several spatial domains and computational meshes. The proposed solvers are the first PIDL methods which solve linear elasticity and hydrodynamic shock-tube problems with high accuracy.

## I. INTRODUCTION

Since the late 1990s, machine learning for scientific computing, also known as scientific machine learning, became a popular research area for scientists worldwide. Most notably, (Lagaris et al., 1998) set the stage by solving differential equations using neural networks. Due to the increase in computational power over the years, a flux of papers has been published discussing various machine learning techniques to solve numerous computational problems. Hence, researchers today incorporate machine learning in several scientific areas, such as extracting physical parameters from experimental data for numerical simulations [18], detecting cracks in the specific regions of a material [17], and, to the interest of this paper, solving a highly nonlinear system of partial differential equations (PDEs) [7].

Of the family of numerical solvers for PDEs that incorporate machine learning, Physics-Informed Neural Networks (PINNs) have proven to be the most popular of these methods. PINNs provide an easy-to-use framework to successfully solve forward and inverse problems, with an impressive degree of accuracy. These features make PINNs a competitive numerical tool compared to standard methods, such as the finite volume method [14] for forward problems and nonlinear least-squares approaches [4] for inverse problems. The developers of PINNs constructed the method to solve "supervised learning tasks while respecting any given law of physics described by a general nonlinear partial differential equation" (Karniadakis et al., 2019). Since the first publication of the method, PINNs became a popular research area in machine learning, and their application to various scientific fields is increasing [11][15][16].

Although PINNs has become a popular method for solving PDEs, it has its limitations as any classical numerical method. These limitations are especially prominent when solving conservation laws whose solutions are discontinuous. However, we expect this difficulty since the universal approximation theorem for neural networks [10][12] specifies that neural networks are universal approximators for solutions to PDEs that are *continuous*. As of today, there is no theoretical backing that generalizes a neural network's ability to approximate any discontinuous solution. Thus, this raises a significant complexity when designing a neural network that will solve a conservation law. For example, the compressible Euler equations describe gas and fluid flow by relating the density, velocity, and pressure to one another. These equations have immense application when modeling shock-tube problems and explosions. The finite volume method (FVM) (LeVeque, 2011) is often the method of choice to solve these problems, but it needs adjustments to its original numerical formulation in order to propagate shock and rarefaction waves correctly. The so-called *flux-limiting* is introduced to resolve artificial dispersion and dissipation created by the FVM schemes. Similarly, PINNs without modifications develop similar phenomena when computing for solutions that include shocks and rarefaction fans. Therefore, for PINNs to be competitive with the FVM with flux-limiting, we must modify the method to solve complicated problems in fluid dynamics, particularly hydrodynamic shock-tube problems.

To the best of my knowledge, (Michoski et al., 2019) and (Patel et al., 2020) are the only other publications introducing modifications to PINNs to solve the classic hydrodynamic shock-tube test problem, the *Sod Shock-Tube Problem* [13]. Both papers discuss modifications to rectify for spurious oscillations near shocks and contact discontinuities, generated by the original PINNs formulation during training. (Michoski et al., 2019) uses artificial viscosity to dissipate oscillations,

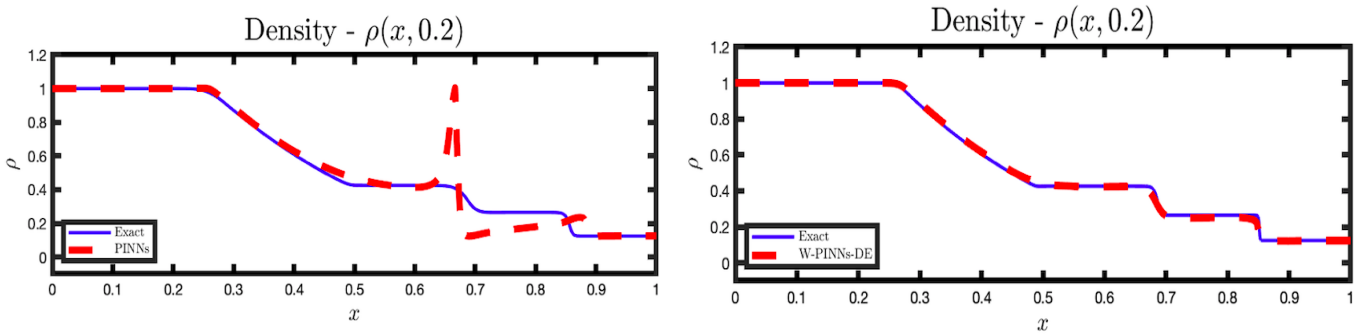


**Figure 1** – The left figure is the solution of the density of the Sod Shock-tube problem using the standard formulation of PINNs. The right figure is the solution of the density of the Sod Shock-tube problem using W-PINNs-DE

by adding viscous terms to the Euler equations. Introducing artificial viscosity is in itself a non-physical adjustment to the mathematical formulation. Adding artificial viscosity stabilizes the solution but at the same time violates, to a certain degree, physical laws in its attempt to capture shocks and rarefaction fans. Moreover, adding artificial viscosity is computationally expensive for neural networks since this requires computing second partial derivatives for each physical quantity, adding computational complexity during backpropagation and automatic differentiation. (Patel et al., 2020) merge a FVM total variation diminishing formulation and artificial viscosity with PINNs. The merger further complicates the PINNs algorithm and, thus, takes away from the simplicity of the PINNs method. Both of these adjustments are designed to solve the specific shock-tube problems addressed in the corresponding papers and do not seem to be easily generalizable to a broader class of shock-tube problems. In this work, we introduce a simple modification to PINNs that allows for solving a broad category of hydrodynamic shock-tube problems with a high degree of accuracy. W-PINNs-DE proves to solve the Sod shock-tube problem more accurately than the methods proposed in the two papers mentioned above. To briefly show the effectiveness of W-PINNs-DE, in figure 1, we offer a side-by-side comparison of the PINNs and W-PINNs-DE solution for the density term of Sod shock-tube problem.

We will test the proposed approach on six hydrodynamic shock-tube test problems. The proposed modifications consists of two components:

- Incorporate weights to the total loss function, such that the loss of the initial condition is minimized faster than the loss of the PDE.
- Extend the original spatial domain to introduce additional training points to the neural network in order to reduce spurious oscillations.

Allowing the loss of initial condition to decrease faster than that of the PDE ensures the neural network learns the initial condition data accurately. Having the neural network learn the initial condition impeccably is essential to minimize the error of the solution at future time,  $t > 0$ . Domain extension smooths out the spurious oscillations by introducing the neural network with more points to the left and right of the initial point of discontinuity,  $x^*$ . The additional training points take on the values of the boundary condition since the boundary conditions for each problem presented are equivalent to the boundaries of the initial condition. The spatial domain extends depending on the initial state,  $\mathbf{U}_0$ .

It is well-established that PINNs have much difficulty resolving boundary conditions for static PDEs with continuous solutions. Although techniques to rectify boundary error have been proposed [19], through numerical experimentation, unfortunately, I found these rectification methods do not generalize to solve plane stress linear elasticity boundary value problems (LEBVP) from solid mechanics (Chen, 2013). Therefore, we use a variation of W-PINNs-DE to solve a LEBVP. We propose to introduce weighting to the total loss function which force the loss of the boundary condition to decrease at a faster rate than the loss of the PDE. However, we will not incorporate domain extension. Therefore, we refer to this modification as W-PINNs.

The rest of the paper is organized as follows. Section II will provide a brief introduction to PINNs, its algorithm, and theoretical limitations. In section III, we present W-PINNs-DE by constructing the method and its algorithm. Section III also discusses the architecture of W-PINNs-DE for each test problem presented in this paper. In sections IV, we solve each of the six hydrodynamic shock-tube test problems using the proposed method, and compare it to the original PINNs formulation, as well as the FVM with flux limiting. Here we will present figures of the solutions, the relative  $L_2$  error for each physical quantity,  $\rho$ ,  $u$ , and  $p$ , and error analysis. In section V, we discuss results presented in section IV and additional error analysis for W-PINNs-DE. In section VI, we shift focus to solve a LEBVP on four spatial domains using W-PINNs. Section VI formulates the LEBVP of interest and the W-PINNs algorithm. Section VII validates W-PINNs by studying the effects of solving the LEBVP on various computational meshes, and mesh refinements. We compare W-PINNs solutions to that of a finite element approximation (FEM) [2]. In section VIII, we discuss results presented in section VII and future work. In the appendix A, we compare Mach numbers and the total energy of W-PINNs-DE solutions with those of the exact solutions, and demonstrate good agreement between them.

Lastly, appendix B compares the W-PINNs calculated strains to that of FEM solutions. All code from this paper is available on Github at: <https://github.com/alexpapados/Physics-Informed-Deep-Learning-Solid-and-Fluid-Mechanics>

## II. BACKGROUND

A. Pinkus proved that a continuous function and its derivatives may be approximated by any single layered (hence a multilayered) neural network (Pinkus, 1999). This theorem suggests and proves that it is possible to approximate a solution to a PDE by using neural networks. Hence, PINNs becomes an eligible method for providing solutions to PDEs as well as their *inverse problems*.

To understand the PINNs formulation, let us consider a general nonlinear PDE:

$$\begin{cases} \frac{\partial \mathbf{u}}{\partial t} + \mathcal{L}(\mathbf{u}) = 0, & (x, t) \in \Omega \times (0, T] \\ \mathbf{u}(x, t) = \mathbf{g}(x, t), & (x, t) \in \partial\Omega \times (0, T] \\ \mathbf{u}(x, 0) = \mathbf{h}(x), & x \in \Omega \end{cases} \quad (1)$$

where  $\mathcal{L}$  is a nonlinear differential operator,  $\Omega \subset \mathbb{R}^d$ , and  $u(x, t)$  is the exact solution to (1). To solve (1) using PINNs, we construct a deep neural network (DNN),  $\tilde{\mathbf{u}}(x, t, \theta)$ , where  $\theta \in \mathbb{R}^k$  are network weights,  $(x, t)$  are inputs to the network, and  $\tilde{\mathbf{u}} = [\tilde{u}_1(x, t), \dots, \tilde{u}_n(x, t)]$  is the output. The standard loss (Karniadakis et al., 2019) is defined by:

$$G(\theta) = \frac{1}{N_f} \left\| \frac{\partial \tilde{\mathbf{u}}}{\partial t}(x, t, \theta) + \mathcal{L}(\tilde{\mathbf{u}}(x, t, \theta)) \right\|_{\Omega \times (0, T], \nu_1}^2 + \frac{1}{N_{IC}} \left\| \tilde{\mathbf{u}}(x, 0, \theta) - \mathbf{h}(x) \right\|_{\Omega, \nu_2}^2 + \frac{1}{N_{BC}} \left\| \tilde{\mathbf{u}}(x, t, \theta) - \mathbf{g}(x, t) \right\|_{\partial\Omega \times (0, T], \nu_3}^2 \quad (2)$$

where  $N_f$ ,  $N_{IC}$ , and  $N_{BC}$  correspond to the number of points sampled from the interior, initial, and boundary conditions, according to their respective probability densities  $\nu_1$ ,  $\nu_2$  and  $\nu_3$ . We then minimize (2) to optimize  $\theta$  through the use of stochastic gradient descent. After an appropriate number of epochs, the neural network should output an approximate solution to (1).

Unfortunately, the theorem of Pinkus does not generalize to solutions to PDEs that are discontinuous. This restricts the current PINNs framework to solve problems with only continuous solutions. Hence, W-PINNs-DE were developed to bypass theoretical and computational limitations of the original PINNs method by approximating solutions of a general class of discontinuous problems referred to as hydrodynamic shock-tube problems.

## III. W-PINNS-DE

### A. Euler Equations

Consider the 1-D compressible Euler equations in characteristic form, where  $\Omega \subset \mathbb{R}$ :

$$\frac{\partial \mathbf{U}}{\partial t} + \mathbf{A} \frac{\partial \mathbf{U}}{\partial x} = 0, \quad (x, t) \in \Omega \times (0, T] \quad (3)$$

where,

$$\mathbf{U} = (\rho, u, p)^T, \quad \mathbf{A} = \begin{pmatrix} u & \rho & 0 \\ 0 & u & \frac{1}{\rho} \\ 0 & \rho a^2 & u \end{pmatrix}$$

where  $a = \sqrt{\gamma p / \rho}$  is the speed of sound,  $\rho$  is the density,  $u$  is the velocity,  $p$  is the pressure, and  $\gamma$  is the heat capacity ratio. For a standard hydrodynamic shock-tube problem, typically, the initial condition is of the form:

$$\mathbf{U}(x, 0) = \mathbf{U}_0 = \begin{cases} \mathbf{u}_L, & x < x^* \\ \mathbf{u}_R, & x > x^* \end{cases}, \quad \mathbf{u}_L = [\rho_L, u_L, p_L], \quad \mathbf{u}_R = [\rho_R, u_R, p_R] \quad (4)$$

with Dirichlet boundary conditions that take the values of the initial condition at the boundaries.

### B. Domain Extension

First, we will discuss what it means to extend the spatial domain of the problem,  $\Omega$ . We extend  $\Omega$  in a manner such that if  $\mathbf{u}_L > \mathbf{u}_R$ ,  $\Omega$  is extended such that the initial state leans to the left of the newly extended spatial domain,  $\Omega_e$ .

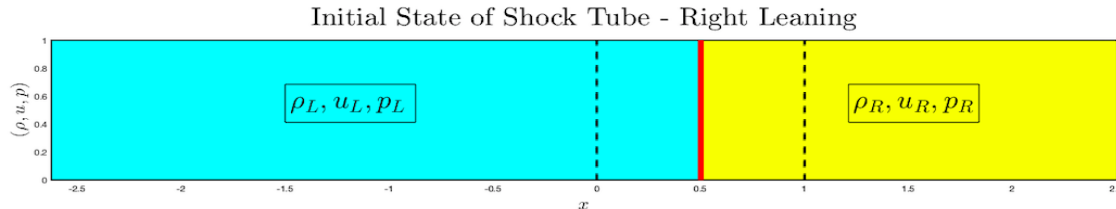


**Figure 2** – An example of domain extension in the reverse Sod problem in section IV.C. The given domain  $[0, 1]$  is extended to  $[-2.625, 2.5]$ .

If  $\mathbf{u}_R > \mathbf{u}_L$ ,  $\Omega$  is extended such that the initial state leans to the right of  $\Omega_e$ . In the case where we have a mixture of initial states, we will extend the spatial domain such that each initial state leans towards the dominant direction of propagation. Since the initial state,  $\mathbf{U}_0$ , varies but remains constant to the right and left of the point of discontinuity,  $x^*$ , we extend  $\Omega$  so the neural network trains on sufficiently many points that remain constant, and hence are easily learned by the network. By the time the neural network reaches  $x^*$  from the right and left, it will encounter a sharp change in gradient (a discontinuous change). My numerous numerical experiments show that extending  $\Omega$  smooths out any artificial oscillations that are typically generated when solving within the original spatial domain. By eliminating spurious oscillations in the solutions, we further minimize the total loss of the neural network. Domain extension in this manner acts as artificial viscosity, but does not introduce any non-physical terms. Therefore, no physical laws are altered or violated. To truly add artificial viscosity, we would need to incorporate  $\rho_{xx}$ ,  $u_{xx}$ , and  $p_{xx}$  into the Euler equations. Adding artificial viscosity is more costly since much of the computation lies in calculating the second derivatives. Therefore, extending the spatial domain with regards to the initial condition is a cheaper and more effective way of diffusing spurious oscillations when solving hydrodynamic shock-tube problems using PINNs. In table I, we define each test problems original domain, and subsequently its newly extended domain based on the initial state of the problem.

Let  $\Omega \equiv (a, b)$  be the original spatial domain, and  $x^* \in \Omega$  is the point of discontinuity from (4). Then, we have the spatial domain transformation:

$$\Omega \longrightarrow \Omega_e$$

where  $\Omega_e = (a_e, b_e)$ . In figure 2, we present a right leaning domain extension.

### C. Weighting

The second modification we make to PINNs consists in introducing weights to the loss function. To solve the Euler equations using PINNs, we construct a deep neural network (DNN),  $\tilde{\mathbf{U}}(x, t, \theta)$ , where  $(x, t)$  are inputs to the network, and  $\tilde{\mathbf{U}} = [\tilde{\rho}, \tilde{u}, \tilde{p}]$  are the outputs. Similarly to (2), the standard loss is defined by:

$$G(\theta) = \frac{1}{N_f} \left\| \frac{\partial \tilde{\mathbf{U}}}{\partial t}(x, t, \theta) + \tilde{\mathbf{A}} \frac{\partial \tilde{\mathbf{U}}}{\partial x}(x, t, \theta) \right\|_{\Omega \times (0, T], \nu_1}^2 + \frac{1}{N_{IC}} \left\| \tilde{\mathbf{U}}(x, 0, \theta) - \mathbf{U}(x, 0) \right\|_{\Omega, \nu_2}^2 + \frac{1}{N_{BC}} \left\| \tilde{\mathbf{U}}(x, t, \theta) - \mathbf{U}(x, t) \right\|_{\partial \Omega \times (0, T], \nu_3}^2 \quad (5)$$

We will refer to the first, second, and third components in (5) as  $G_f(\theta)$ ,  $G_{IC}(\theta)$ , and  $G_{BC}(\theta)$ , respectively. Since the boundary conditions are induced by the initial conditions, we drop boundary condition term in (5). Hence,

$$G(\theta) = G_f(\theta) + G_{IC}(\theta) \quad (6)$$

Our numerical experiments have shown that the PDE loss  $G_f(\theta)$  decreases at a faster rate than the initial condition loss  $G_{IC}(\theta)$  when using (5) and (6). This means that the neural network learns an arbitrary solution to the PDE and then tries to adjust it at all interior training points and all times  $(x_n, t_n)$  to fit the initial condition. The Euler equations are of hyperbolic type which means that it, in essence, propagates the initial condition through the domain, possibly modifying its shape. Therefore, if the initial condition is not learned correctly, the solution in the whole time interval tends to be substantially different from the correct one. The reason for slow learning of the initial condition seems to be the discontinuity in the initial state. Indeed, we are forcing a smooth function (the DNN) to approximate a discontinuous function.

We propose to introduce weights in order to reverse this situation. Giving a large weight to the initial condition loss  $G_{IC}(\theta)$  forces the neural network to fit the initial condition first and then adjust the solution to satisfy the PDE at later times.

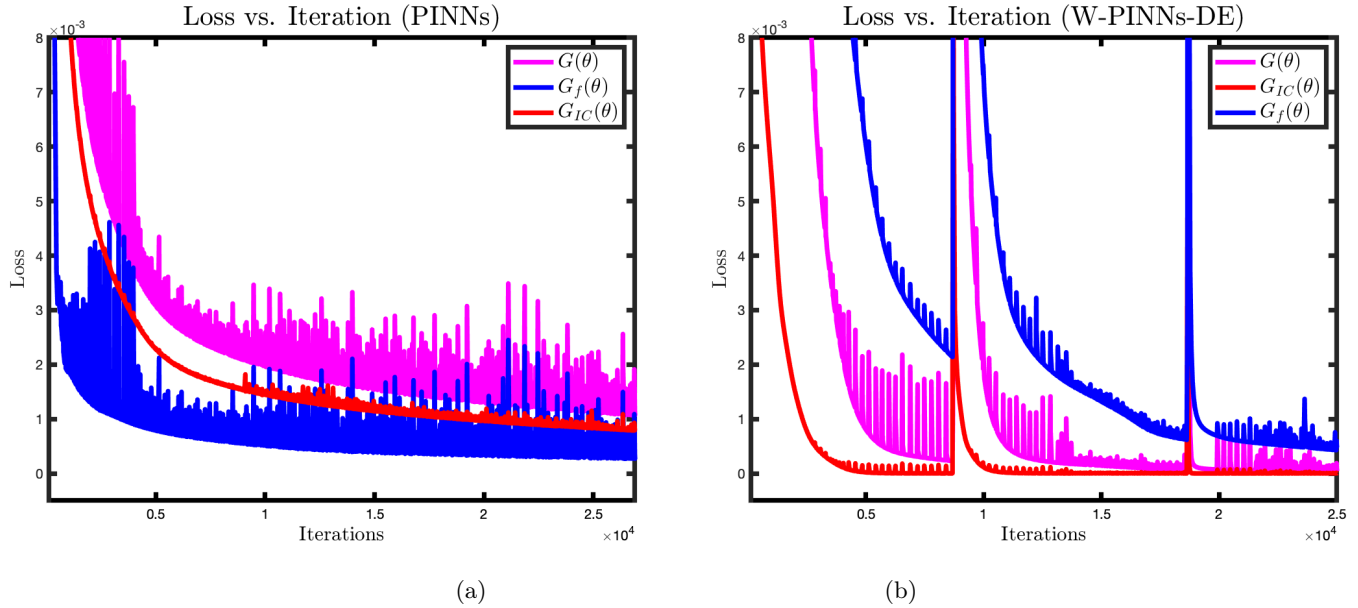


**Figure 3 – Loss vs. Iteration: PINNs (a), W-PINNs-DE (b)**

We observe that as the initial condition is nearly satisfied by the neural network, then the whole solution is learned considerably faster. The proposed loss function is of the form

$$G(\theta) = \omega_f G_f(\theta) + \omega_{IC} G_{IC}(\theta) \quad (7)$$

where  $\omega_{IC} \gg \omega_f$ . We have used  $\omega_f = 0.1$  and  $\omega_{IC} = 10$ . Our numerical experiments with various weight combinations have shown that setting  $\omega_{IC}$  to be 100 times greater than  $\omega_f$  is optimal for training.

With the choice of weights,  $\omega_f$ ,  $\omega_{IC}$  and the proper domain extension, if the initial state does not contain strong shocks, (i.e  $\|\mathbf{U}_0\|^2 > 10$ , or blast waves), we expect the following inequality for a sufficient number of epochs (training iterations):

$$0 \leq G_{IC}(\theta) \leq G_f(\theta) \quad \forall \theta \in \mathbb{R}^k \quad (8)$$

W-PINNs-DE maintains this inequality by the end of its training, as well as an accurate solution of a hydrodynamic shock-tube problem. Figure 1 presents the solution of the density of the Sod shock-tube problem. PINNs failure to capture the shock and contact-discontinuity results from an inability to satisfy (8). In figure 3, we compare  $G(\theta)$ ,  $G_f(\theta)$ , and  $G_{IC}(\theta)$  versus training iterations for PINNs and W-PINNs-DE when solving the Sod shock-tube problem. For each iteration, W-PINNs-DE satisfy (8) whereas PINNs do not. In Figure 3(b), we observe occasional large spikes occurring in the process of training of W-PINNs-DE. We believe that they are due to occasional choice of unfortunate directions by the stochastic gradient descend and large amplification of their effect due to the large weight of  $G_{IC}$ . However, the learning process quickly returns back on the desired track.

#### D. W-PINNs-DE Architecture

For each problem presented in table I, we sample points from the extended computational domain that has been partitioned into 1000 points in  $x$  and 1000 points in  $t$ . We represent the computational domain by  $N_{x,t} = \{1000, 1000\}$ . Each neural network has 7 layers with 30 neurons per layer, uses the  $\tanh(\cdot)$  activation function for non-linear layers, and a learning rate of 0.0005. Taking less than 7 layers resulted in high approximation error and solutions of no physical meaning. Increasing the number of layers makes the numerical solution more accurate but also increases the computational cost. We have found that a DNN with 7 layers yields a good compromise between the accuracy and the computational cost. In order to validate the use of the  $\tanh(\cdot)$  activation function, various activation functions such as RELU and sigmoid were utilized for each shock-tube problem. However, the  $\tanh(\cdot)$  activation function proved most suitable for allowing neural networks to approximate solutions to hydrodynamic shock-tube problems. Lastly, we use the ADAM optimizer for stochastic gradient descent. In table I, we present the test shock-tube problem, the number of epochs for training the neural network, the original domain, and the transformed extended domain.

PyTorch is a useful package for data science and machine learning. It provides easy-to-use functions for training, backpropagation, and auto-differentiation. Hence, all W-PINNs-DE code was written using PyTorch, and therefore, Python was the only coding language used to obtain W-PINNs-DE solutions for the findings of this paper. Numerical solutions using classical numerical methods and analytic solutions were obtained using C++ and MATLAB.

Problem	Epochs	Original Domain, $\Omega \times (0, T]$	Extended Domain, $\Omega_e \times (0, T]$
Single Contact Discont.	44,350	$[0, 1] \times [0, 2]$	$[-2.6175, 2.5] \times [0, 2]$
Double Expansion Fan	40,165	$[0, 1] \times [0, 0.2]$	$[-2.625, 2.5] \times [0, 0.2]$
Sod shock-tube	76,140	$[0, 1] \times [0, 0.2]$	$[-1.5, 3.125] \times [0, 0.2]$
Reverse Sod shock-tube	76,140	$[0, 1] \times [0, 0.2]$	$[-2.625, 2.5] \times [0, 0.2]$
High-speed shock-tube I	55,765	$[-0.5, 1.5] \times [0, 0.2]$	$[-2.625, 2.5] \times [0, 0.2]$
High-speed shock-tube II	67,200	$[0, 1] \times [0, 0.2]$	$[-2.625, 3.125] \times [0, 0.2]$

**Table I** – Test shock-tube problem, the number of epochs for training the neural network, the original domain, and the extended domain

### E. W-PINNs-DE Algorithm

To summarize, W-PINNs-DE extends the original domain so the neural network trains on additional points that take on the values of the boundary condition and the boundaries of the initial condition. These additional training points are cause smoothing oscillations near points of discontinuity and, thus, minimize the total loss more efficiently. Extending the spatial domain acts as artificial viscosity for neural networks, but without introducing non-physical terms to the mathematical model. W-PINNs-DE then penalize the total loss function by introducing weights that allow  $G_{IC}(\theta)$  to decrease at a faster rate than  $G_f(\theta)$ . See **Algorithm 1** below.

---

#### Algorithm 1: W-PINNs-DE ALGORITHM

---

- 1 Extend  $\Omega$  based on the initial state (left or right leaning).
- 2 Generate weights  $\theta \in \mathbb{R}^k$  and a deep neural network (DNN),  $\tilde{\mathbf{U}}(x, t, \theta)$ , where  $(x, t)$  are inputs to the network, and  $\tilde{\mathbf{U}} = [\tilde{\rho}, \tilde{u}, \tilde{p}]$  are the outputs. The number of layers, neurons per layer, and activation functions for each layer are prescribed by the user.
- 3 Generate random points  $(x_n, t_n)$  from  $\Omega \times \mathbb{R}^+$  and  $w_n$  from  $\Omega$ , according to their respective probability densities,  $\nu_1$  and  $\nu_2$ . Let  $N_f, N_{IC}$  correspond to the number of points sampled from the interior and initial condition, respectively.
- 4 Define the loss function as:

$$G(\theta) = \frac{\omega_f}{N_f} \left\| \frac{\partial \tilde{\mathbf{U}}}{\partial t}(x, t, \theta) + \tilde{\mathbf{A}} \frac{\partial \tilde{\mathbf{U}}}{\partial x}(x, t, \theta) \right\|_{\Omega \times (0, T], \nu_1}^2 + \frac{\omega_{IC}}{N_{IC}} \left\| \tilde{\mathbf{U}}(x, 0, \theta) - \mathbf{U}(x, 0) \right\|_{\Omega, \nu_2}^2$$

where  $\omega_f = 0.1$ ,  $\omega_{IC} = 10$

- 5 Update  $\theta$  by performing stochastic gradient descent:

$$\theta = \theta - \eta \nabla_{\theta} G(\theta)$$

where  $\eta$  is the learning rate.

---

## IV. HYDRODYNAMIC SHOCK-TUBE TEST PROBLEMS

In this section, we compare the performance of W-PINNs-DE to those of the original PINNs formulation, and the finite volume method (FVM) with flux limiting. We will use the HLLE flux solver, with the Osher flux limiter, and RK-3 for time integration for FVM solutions [14]. When solving each test problem using W-PINNs-DE and PINNs, we sample the same number of points from the computational domain  $N_{x,t} = \{1000, 1000\}$ . To make a fair comparison, we partition the spatial moment for the FVM to 1000 points as well. However, the time step in each test problem is chosen to satisfy the CFL stability condition, and therefore varies from problem to problem.

For each numerical solution, we measure the relative  $L_2$  error between the W-PINNs-DE solution and an analytic solution or a refined FVM solution. Specifically, we measure:

$$\mathcal{E} = \frac{\sum_{n=1}^{N_{x,t}} \|\tilde{\mathbf{U}}(x_n, t_n, \theta) - \mathbf{U}(x_n, t_n)\|_2}{\sum_{n=1}^{N_{x,t}} \|\mathbf{U}(x_n, t_n)\|_2}$$

where  $(x_n, t_n)$  belong to the computation domain,  $N_{x,t}$ . The initial data for the six test problems for the Euler equation (3) with initial conditions of the form (4) are listed in Table II.

Problem	$\rho_L$	$u_L$	$p_L$	$\rho_R$	$u_R$	$p_R$	$x^*$
Single Contact Discontinuity	1.4	0.1	1.0	1.0	0.1	1.0	0.5
Double Expansion Fan	1.0	-1.0	0.4	1.0	1.0	0.4	0.5
Sod Shock-Tube Problem	1.0	0.0	1.0	0.125	0.0	0.1	0.5
Reverse Shock-Tube Problem	0.125	0.0	0.1	1.0	0.0	1.0	0.5
High Speed Shock-Tube I	0.125	0.0	0.1	1.0	0.75	1.0	0.3
High Speed Shock-Tube II	0.445	0.698	0.70	0.5	0.0	0.571	0.5

Table II – Initial data for the six hydrodynamic shock-tube problems to validate W-PINNs-DE ability to solve (3) -(4)

### A. Single Contact Discontinuity Problem

The single contact discontinuity problem is the simplest hydrodynamic shock-tube problem we consider. As shown in table II, the initial state of the density is greater on the left of  $x^*$  than on the right, while the velocity and pressure remain constant. In this case, the initial density profile, a step function, propagates with the shock speed, while its shape remains unchanged. In figure 4, we compare W-PINNs-DE with PINNs and the FVM to demonstrate their ability to capture the initial and final state of the density. Table IV reveals the relative  $L_2$  errors for the density, velocity, and pressure solutions of each method.

We remark that obtaining an accurate numerical solution to this problem presents a challenge for numerical methods. Finite volume methods typically introduce dispersion or dissipation near points of discontinuity. The FVM creates immense dissipation at the final time,  $t = 2.0$ . Moreover, the FVM with flux limiting requires a heavily refined mesh to resolve the final contact discontinuity. Figure 4 demonstrates W-PINNs-DE ability to capture the contact discontinuity with minimal dissipation and dispersion, and without an immensely refined mesh. Although the original PINNs method has a smaller relative  $L_2$  error for the density than the FVM, dispersion at the top and bottom of the discontinuity is apparent for each  $t$ . In table IV, we find that W-PINNs-DE has the smallest error for the density in comparison to the other methods, resulting from minimal dispersion and dissipation for each  $t$ . Despite the fact the FVM solves for the velocity and pressure more accurately than W-PINNs-DE and PINNs, it is important to recognize that the FVM does not learn the initial condition, whereas W-PINNs-DE and PINNs trains to fit the initial data. Therefore, if the FVM has error at the initial condition, this is simply machine error, whereas W-PINNs-DE and PINNs accumulates approximation error from training or fitting the initial condition.

$\rho_L$	$u_L$	$p_L$	$\rho_R$	$u_R$	$p_R$	$x \in \Omega$	$x \in \Omega_e$	$x^*$
1.4	0.1	1.0	1.0	0.1	1.0	(0, 1)	(-2.6175, 2.5)	0.5

Table III – Initial conditions for the single contact discontinuity problem

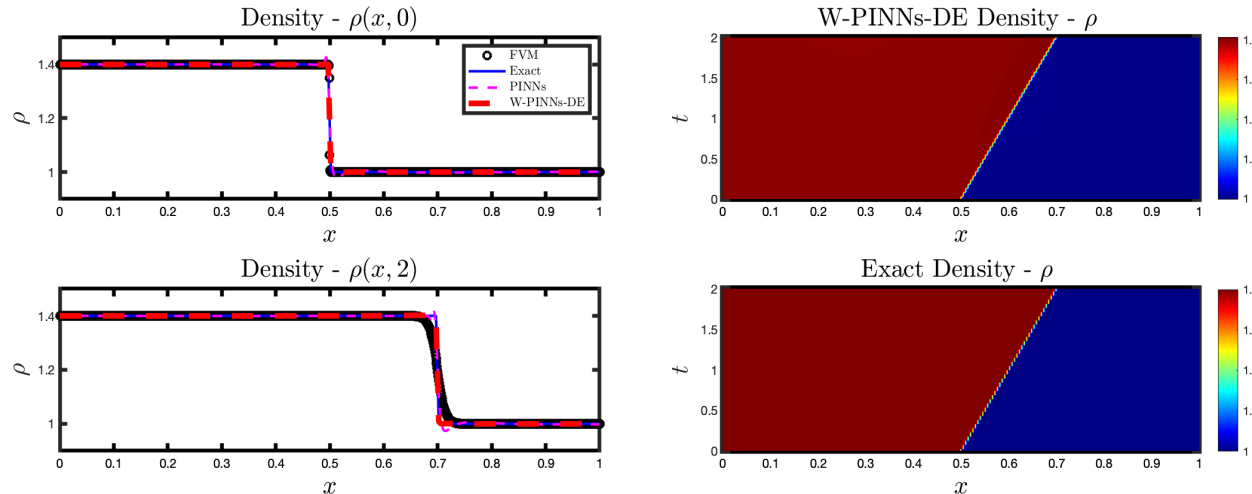


Figure 4 – Upper: The initial state of the density at  $t = 0$  (left). The W-PINNs-DE solution of the density at  $(x, t)$  (right). Lower: Solution of the density at final time,  $t = 2.0$  (left). The exact solution of the density at  $(x, t)$ . W-PINNs-DE and PINNs had sample sizes of  $N_f = 20,000$ , and  $N_{IC} = 1,000$

Method	$\frac{\ \rho_{approx} - \rho_{exact}\ _2}{\ \rho_{exact}\ _2}$	$\frac{\ u_{approx} - u_{exact}\ _2}{\ u_{exact}\ _2}$	$\frac{\ p_{approx} - p_{exact}\ _2}{\ p_{exact}\ _2}$
FVM	$3.5e - 03$	$5.3e - 05$	$3.6e - 06$
PINNs	$1.1e - 03$	$1.3e - 03$	$8.4e - 04$
W-PINNs-DE	$1.6e - 04$	$1.2e - 04$	$1.6e - 04$

Table IV – Relative  $L_2$  error for the single contact discontinuity problem

### B. Sod Shock-Tube Problem

The Sod shock-tube problem [13] is a standard hydrodynamic shock-tube test problem. The Sod problem is often used as a test problem to validate the ability of numerical methods to capture characteristics unique to solving conservation laws. The solution for each physical quantity develops a rarefaction fan, contact discontinuity, and shock. As mentioned in section III.A, numerically computing the shock, contact discontinuity and rarefaction fan is difficult, as artificial dispersion or dissipation is created near points of discontinuity by the numerical scheme. Therefore, designing a scheme that captures each discontinuous component is essential in order to obtain accurate numerical solutions.

In figure 5, W-PINNs-DE captures each discontinuous component for both the density and pressure terms with ease. Although the velocity is approximated quite well, we see an acceptable amount of dissipation near the right shock. In table VI, we find the relative  $L_2$  error for the W-PINNs-DE density and pressure is less than 0.8%, while the relative  $L_2$  error for the velocity is less than 6%. Typically, solving numerically for the velocity field of a shock-tube problem is challenging. Hence, a relative  $L_2$  error of less 6% error is acceptable and competitive with respect to classical numerical solvers. W-PINNs-DE performs slightly better than the FVM, whereas the standard PINNs method creates immense dispersion at the contact discontinuity and shock, resulting in a large  $L_2$  error for each physical quantity. Moreover, W-PINNs-DE solves this problem more accurately, and in a simpler manner than both the (Michoski et al., 2019) and the (Patel et al., 2020) reported schemes.

$\rho_L$	$u_L$	$p_L$	$\rho_R$	$u_R$	$p_R$	$x \in \Omega$	$x \in \Omega_e$	$x^*$
1.0	0.0	1.0	0.125	0.0	0.1	(0,1)	(-1.5,3.125)	0.5

Table V – Initial conditions for the Sod shock-tube problem

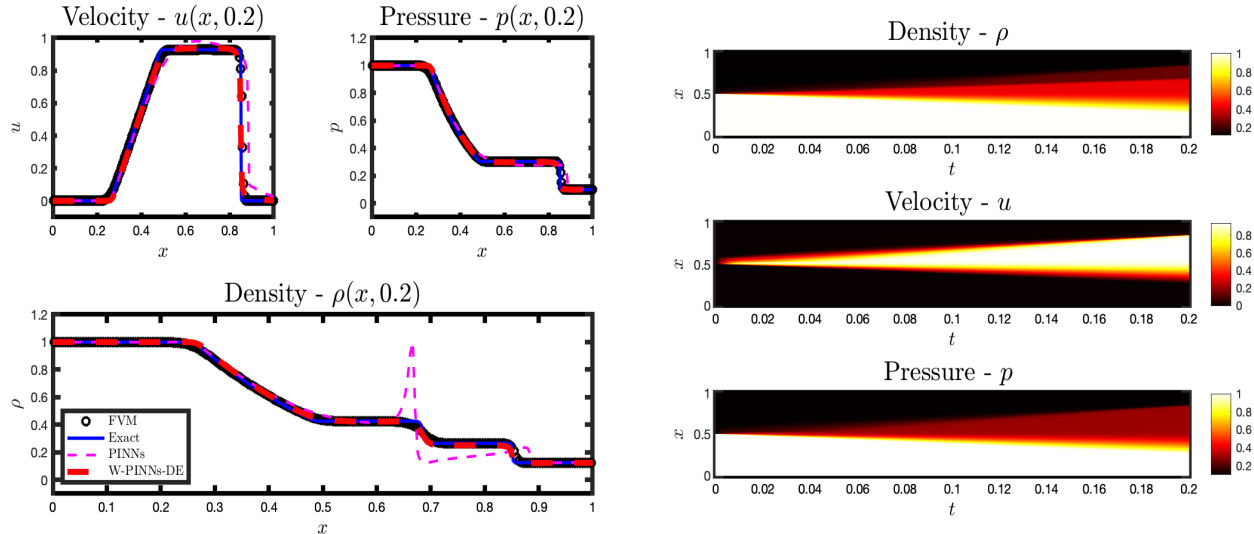


Figure 5 – Left: Solution of the velocity, pressure, and density at final time,  $t = 0.2$ . Right: W-PINNs-DE solution of each physical quantity at  $(x, t)$ . W-PINNs-DE and PINNs had sample sizes of  $N_f = 11,000$ ,  $N_{IC} = 1,000$ .

Method	$\frac{\ \rho_{approx} - \rho_{exact}\ _2}{\ \rho_{exact}\ _2}$	$\frac{\ u_{approx} - u_{exact}\ _2}{\ u_{exact}\ _2}$	$\frac{\ p_{approx} - p_{exact}\ _2}{\ p_{exact}\ _2}$
FVM	$8.7e - 03$	$4.9e - 02$	$8.7e - 03$
PINNs	$1.2e - 01$	$2.4e - 01$	$5.8e - 02$
W-PINNs-DE	$8.6e - 03$	$5.1e - 02$	$7.2e - 03$

Table VI – Relative  $L_2$  error for the Sod shock-tube problem

### C. Reverse Sod Shock-Tube Problem

The reverse Sod shock-tube problem reflects the initial state of the classical Sod shock-tube problem so that the initial density and pressure are now greater to the right of  $x^*$  than the left. Similar to the classical Sod shock-tube problem, W-PINNs-DE captures the shock, contact discontinuity, and rarefaction fan for the density and pressure with ease, whereas the velocity solution experiences an acceptable amount of dissipation near the shock. Table VIII reveals W-PINNs-DE outperforms PINNs and the FVM. PINNs experience immense dispersion at the shock, resulting in a high relative  $L_2$  error. The FVM and W-PINNs-DE add slight dissipation at the contact discontinuity, but W-PINNs-DE proves to capture the shock and rarefaction fan more accurately and without a heavily refined mesh.

Interestingly, PINNs and W-PINNs-DE obtain more accurate results for the reverse Sod shock-tube problem than the original problem, whereas the FVM performs worse. Numerical experiments validated the use of the  $\tanh(\cdot)$  activation function in comparison to other functions such as RELU and sigmoid. The  $\tanh(\cdot)$  activation function proved to be most suitable for allowing neural networks to approximate solutions to hydrodynamic shock-tube problems. It is speculated that the geometry of the  $\tanh(\cdot)$  activation function allows the neural network to solve the reverse problem more efficiently. It seems that the geometry of the  $\tanh(\cdot)$  activation function closely resembles the rarefaction section for each physical quantity, suggesting that activation function geometry may play a role in achieving smaller approximation error. In future work, we will investigate the geometric effects activation functions have on PINNs when solving hydrodynamic shock-tube problems.

$\rho_L$	$u_L$	$p_L$	$\rho_R$	$u_R$	$p_R$	$x \in \Omega$	$x \in \Omega_e$	$x^*$
0.125	0.0	0.1	1.0	0.0	1.0	(0, 1)	(-2.625, 2.5)	0.5

Table VII – Initial conditions for the reverse Sod shock-tube problem

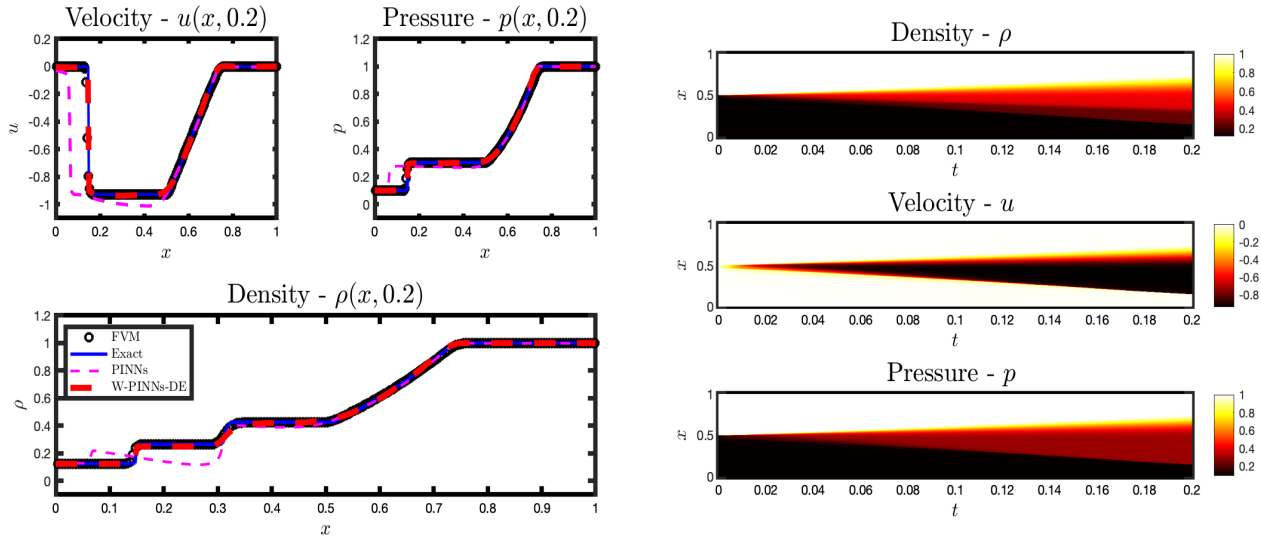


Figure 6 – Left: Solution of the velocity, pressure, and density at final time,  $t = 0.2$ . Right: W-PINNs-DE solution of each physical quantity at  $(x, t)$ . W-PINNs-DE and PINNs had sample sizes of  $N_f = 10,500$ ,  $N_{IC} = 1,000$ .

Method	$\frac{\ \rho_{approx} - \rho_{exact}\ _2}{\ \rho_{exact}\ _2}$	$\frac{\ u_{approx} - u_{exact}\ _2}{\ u_{exact}\ _2}$	$\frac{\ p_{approx} - p_{exact}\ _2}{\ p_{exact}\ _2}$
FVM	$9.4e - 03$	$3.0e - 02$	$1.0e - 02$
PINNs	$3.7e - 02$	$2.1e - 01$	$4.1e - 02$
W-PINNs-DE	$8.5e - 03$	$3.0e - 02$	$6.6e - 03$

Table VIII – Relative  $L_2$  error for the reverse Sod shock-tube problem

#### D. Double Expansion Fan Problem

In the double expansion fan problem, the density and pressure are initially constant and continuous, while the initial velocity is greater to the right of  $x^*$  compared to the left. Unlike the single contact discontinuity problem, we observe that the double rarefaction fan problem does not simply translate the initial discontinuity. Instead, each physical quantity develops two, oppositely traveling, expansion fans. Figure 7 demonstrates that each physical quantity evolves to have two expansion fans.

In figure 7, we compare W-PINNs-DE to PINNs and the FVM, as done in previous sections. W-PINNs-DE solves this problem more accurately than PINNs and the FVM, as shown in table X. Remarkably, the original PINNs method shows no difficulty to solve this problem, as it obtains less than 0.6% relative  $L_2$  error for each physical quantity. The neural network does not have difficulty approximating the solution since sharp jumps are not present as  $t$  approaches the final time,  $T = 0.2$ . However, in figures 7 and 8, we see that PINNs dissipates the solution near the smoothed corners towards the boundary, resulting in the highest relative  $L_2$  error in comparison to the other methods. On the other hand, the FVM slightly disperses the solution at  $x = 0.5$ . At  $x = 0.5$ , the two fans depart, hence, the solution is prone to higher error at  $(0.5, t)$ , for  $t > 0$ . W-PINNs-DE proves to have minimal dispersion and dissipation, resulting in having the smallest relative  $L_2$  error.

$\rho_L$	$u_L$	$p_L$	$\rho_R$	$u_R$	$p_R$	$x \in \Omega$	$x \in \Omega_e$	$x^*$
1.0	-1.4	0.1	1.0	1.0	0.4	$(0, 1)$	$(-2.625, 2.5)$	0.5

Table IX – Initial conditions for the double expansion fan problem

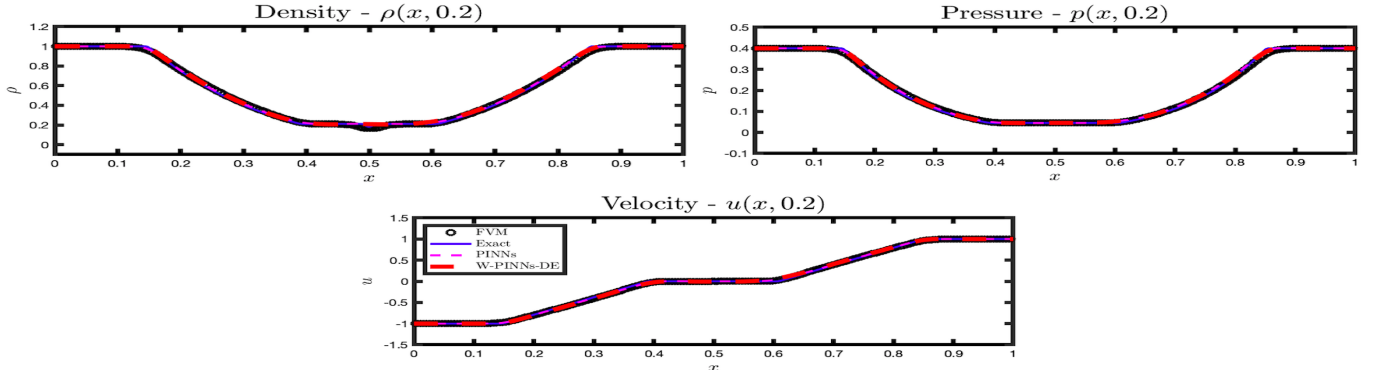


Figure 7 – Solution at  $t = 0.2$  for the double expansion fan problem, with sampled points,  $N_f = 10,500$ ,  $N_{IC} = 1,000$

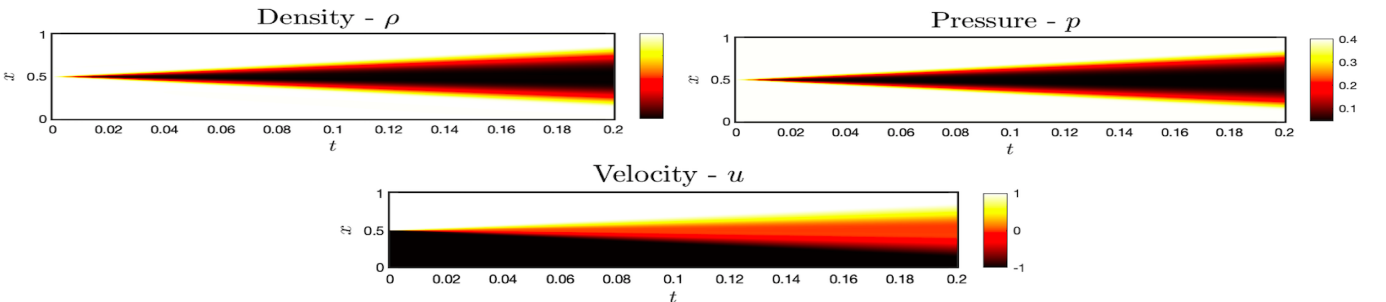
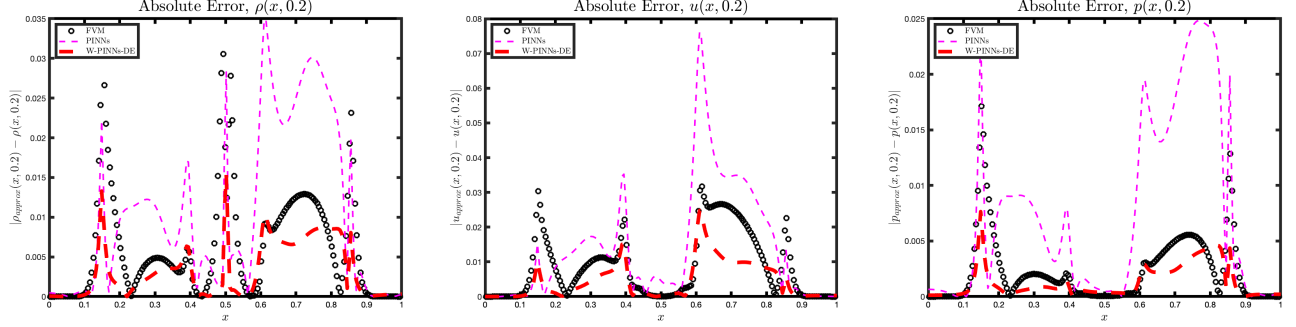


Figure 8 – Top view of solution to the double expansion fan problem

Figure 9 – Absolute error at  $t = 0.2$ 

Method	$\frac{\ \rho_{approx} - \rho_{exact}\ _2}{\ \rho_{exact}\ _2}$	$\frac{\ u_{approx} - u_{exact}\ _2}{\ u_{exact}\ _2}$	$\frac{\ p_{approx} - p_{exact}\ _2}{\ p_{exact}\ _2}$
FVM	$2.7e - 03$	$2.1e - 03$	$1.9e - 03$
PINNs	$4.5e - 03$	$3.2e - 03$	$5.2e - 03$
W-PINNs-DE	$1.4e - 03$	$1.6e - 03$	$1.3e - 03$

Table X – Relative  $L_2$  errors for double expansion fan problem

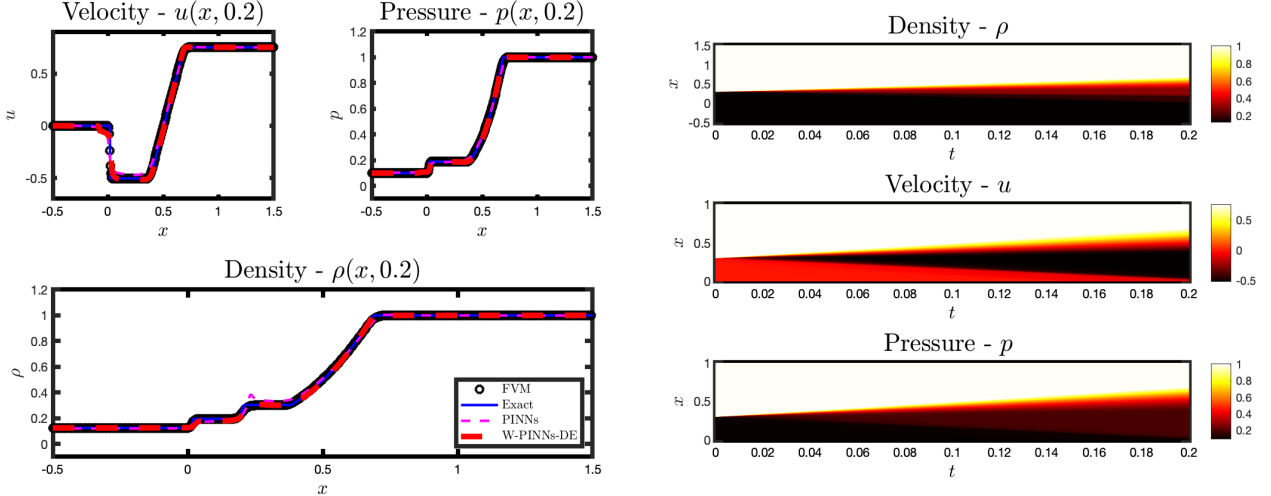
### E. High-Speed Flow Problem I

The first high-speed flow problem we consider is a modified reverse Sod shock-tube problem. The initial state of the density and pressure are equivalent to that of the reverse Sod shock-tube problem, but now the initial velocity is greater on the right of  $x^*$  than the left. Although the modified reverse Sod shock-tube problem has an additional discontinuous initial state, the relative  $L_2$  errors are smaller than that of the reverse Sod shock-tube problem.

W-PINNs-DE and the FVM create some amount of artificial dissipation at the contact discontinuity, whereas PINNs disperses the solution, as shown in figure 10 and 11. PINNs have a higher relative  $L_2$  error for each physical quantity since it disperses the solution in several regions. Although W-PINNs-DE has the smallest relative  $L_2$  error, in figure 10 and 11, we see there is slight dissipation at the shock and contact discontinuity.

$\rho_L$	$u_L$	$p_L$	$\rho_R$	$u_R$	$p_R$	$x \in \Omega$	$x \in \Omega_e$	$x^*$
0.125	0.0	0.1	1.0	0.75	1.0	(-0.5, 1.5)	(-2.625, 2.5)	0.3

Table XI – Initial conditions for the high-speed flow problem I

Figure 10 – Left: Solution of the velocity, pressure, and density at final time,  $t = 0.2$ . Right: W-PINNs-DE solution of each physical quantity at  $(x, t)$ . W-PINNs-DE and PINNs had sample sizes of  $N_f = 10,500$ ,  $N_{IC} = 1,000$

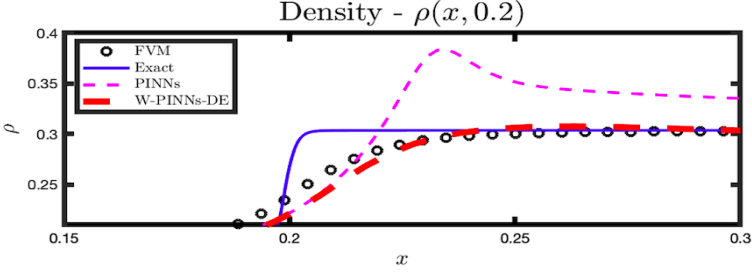


**Figure 11** – Zoom-in of the contact discontinuity of the density from figure 10

Method	$\frac{\ \rho_{approx} - \rho_{exact}\ _2}{\ \rho_{exact}\ _2}$	$\frac{\ u_{approx} - u_{exact}\ _2}{\ u_{exact}\ _2}$	$\frac{\ p_{approx} - p_{exact}\ _2}{\ p_{exact}\ _2}$
FVM	$7.7e - 03$	$3.5e - 02$	$8.1e - 03$
PINNs	$2.2e - 02$	$6.6e - 02$	$1.6e - 02$
W-PINNs-DE	$6.7e - 03$	$3.2e - 02$	$5.0e - 03$

**Table XII** – Relative  $L_2$  errors for High-Speed Flow Problem I

#### F. High Speed Flow Problem II

The second high speed flow problem has the most complex initial state out of all the problems presented in this paper. The reason for this intricacy is due to the fact that this specific shock-tube problem has mixed initial states, where  $\rho_R > \rho_L$ , and  $[u_L, p_L] > [u_R, p_R]$ . In figure 12, W-PINNs-DE captures each rarefaction fan and shock with minimal dissipation and dispersion. The FVM creates slight dissipation in the shock regions of the density, where as the original PINNs method dissipates the solution at the bottom of the shock, but disperses the solution at the top. As reported in table XIV, W-PINNs-DE solves for the density and pressure terms with less than 0.8% error, respectively, and the velocity term with less than 2%. Similarly to the first high-speed flow problem, we are surprised to see how well each method performs considering the complexity of the initial-state in comparison to each test problem presented so far.

$\rho_L$	$u_L$	$p_L$	$\rho_R$	$u_R$	$p_R$	$x \in \Omega$	$x \in \Omega_e$	$x^*$
0.445	0.698	0.7	0.5	0.0	0.571	(0, 1)	(−2.625, 3.125)	0.5

**Table XIII** – Initial conditions for the high-speed flow problem II

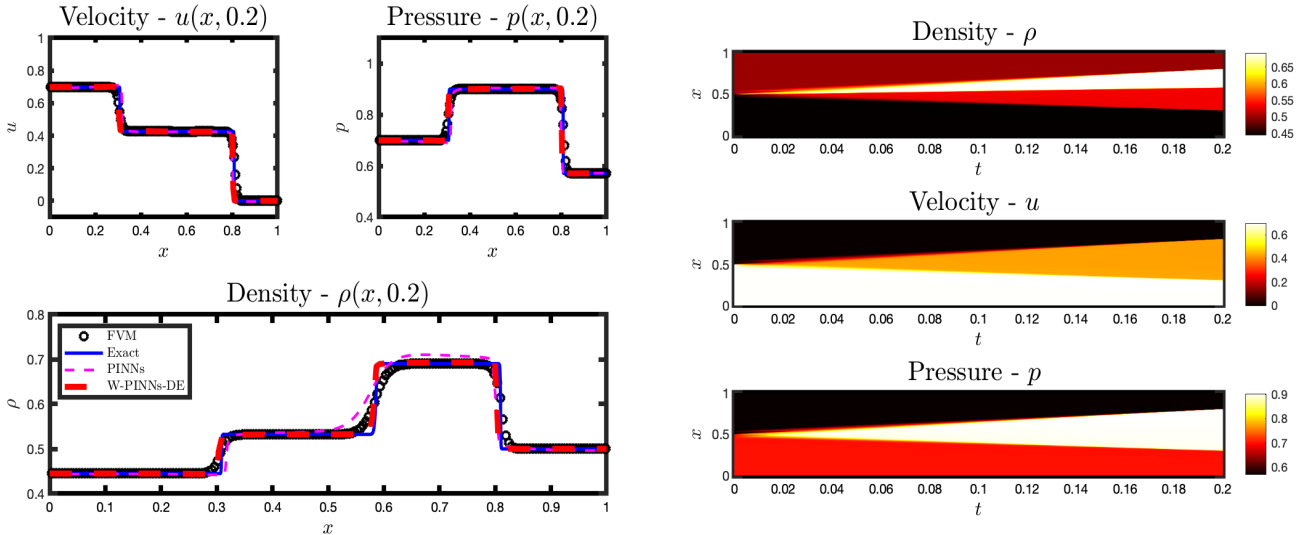


**Figure 12** – Left: Solution of the velocity, pressure, and density at final time,  $t = 0.2$ . Right: W-PINNs-DE solution of each physical quantity at  $(x, t)$ . W-PINNs-DE and PINNs had sample sizes of  $N_f = 11,000$ ,  $N_{IC} = 1,000$

Method	$\frac{\ \rho_{approx} - \rho_{exact}\ _2}{\ \rho_{exact}\ _2}$	$\frac{\ u_{approx} - u_{exact}\ _2}{\ u_{exact}\ _2}$	$\frac{\ p_{approx} - p_{exact}\ _2}{\ p_{exact}\ _2}$
	$\ \rho_{approx} - \rho_{exact}\ _2$	$\ u_{approx} - u_{exact}\ _2$	$\ p_{approx} - p_{exact}\ _2$
FVM	$8.1e - 03$	$3.5e - 02$	$3.5e - 03$
PINNs	$8.7e - 02$	$6.6e - 02$	$4.4e - 02$
W-PINNs-DE	$7.7e - 03$	$1.4e - 02$	$6.9e - 03$

Table XIV – Relative  $L_2$  errors for High-Speed Flow Problem II

## V. DISCUSSION I

In this study, we propose two modifications to the PINNs (Karniadakis et al., 2019) to make them more amenable for solving hydrodynamic shock-tube problems; domain extension and weighting for the loss function. We call the resulting method W-PINNs-DE to reflect these changes. For each test problem, we compared W-PINNs-DE to the FVM with flux limiting [14] and the original PINNs method [7]. Using W-PINNs-DE provides neural networks with a framework to solve for a general class of discontinuous solutions of the compressible Euler equations. It does so by having an ability to capture physical phenomena such as shocks, contact discontinuities, and rarefaction fans, more accurately than the original PINNs and comparably or more accurately than the traditional finite volume methods with flux delimiters. By introducing a weighted loss function and domain extension, we've shown that  $G_f(\theta)$  decreases at a slower rate than  $G_{IC}(\theta)$ , resulting in accurate solutions to hydrodynamic shock-tube problems. To demonstrate the necessity of (8), in figure 3, we plotted the  $G(\theta)$ ,  $G_f(\theta)$ , and  $G_{IC}(\theta)$  versus iteration for PINNs and W-PINNs-DE, when solving the Sod shock-tube problem, and presented their solutions in section III.B.  $G_f(\theta)$  and  $G_{IC}(\theta)$  satisfied (8) for each test problem solved by W-PINNs-DE, whereas PINNs did not. We have shown through each test case that  $G_f(\theta)$  and  $G_{IC}(\theta)$  must satisfy (8) in order to solve hydrodynamic shock-tube problems using neural networks.

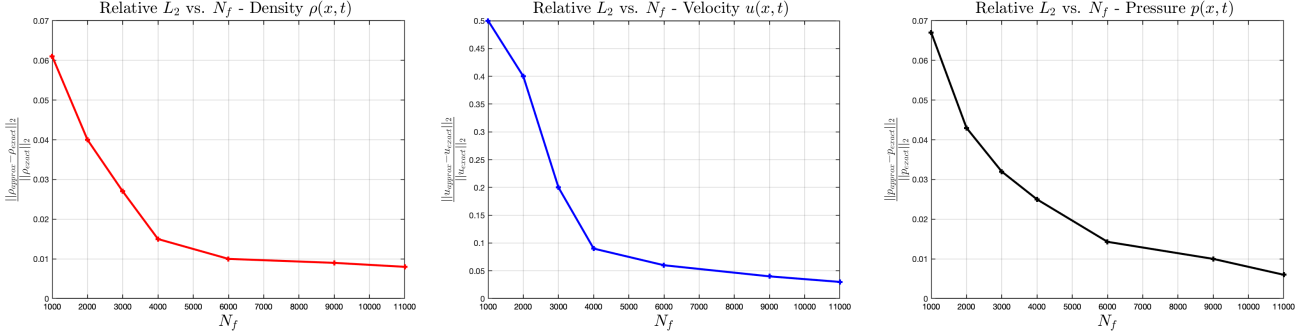


Figure 13 – Relative  $L_2$  errors vs.  $N_f$  samples

Although W-PINNs-DE proves to be a competitive numerical tool for solving conservation laws, each test problem demonstrated higher numerical error for the velocity than the density and pressure. In figures 6-10, the W-PINNs-DE velocity typically experienced dissipation near shock corners, whereas W-PINNs-DE captured the rarefaction fan exceptionally. Though this error is acceptable, it is a goal to find as accurate solutions as possible. Hence, understanding this phenomenon is an essential task. Moreover, we desire a rigorous explanation as to why W-PINNs-DE captures these solutions to such accuracy compared to classical PINNs and other modifications to the method.

The high-speed flow problems presented in sections III.E and III.F had three discontinuous initial states. Both problems developed more physics in their solutions than the other shock-tube problems. Yet, despite the initial state and final solutions complexity, W-PINNs-DE approximates the solution to each high-speed flow problem with smaller relative  $L_2$  error than W-PINNs-DE solutions to the Sod shock-tube problems. To get an idea of how W-PINNs-DE error decays as  $N_f$  increases, in figure 13, we plot the relative  $L_2$  errors versus  $N_f$  for the high speed flow problem II. It is to be expected that as  $N_f$  increases, the relative  $L_2$  error for each physical quantity will decrease. As the number of samples increases, the neural network resolves the solution accurately. However, figure 13 reveals for  $N_f \geq 9,000$ , the relative  $L_2$  errors reach a saturation point. In future work, we will investigate rigorously the convergence of W-PINNs-DE.

To summarize, this study demonstrated that W-PINNs-DE solves complex shock-tube problems. Moreover, W-PINNs-DE yields higher accuracy on a class of hydrodynamic shock-tube problems than other PINNs and finite volume methods, making it a competitive numerical tool suited in tackling conservation laws. In addition to solving hydrodynamic shock-tube problems, W-PINNs-DE can solve isothermal Euler equations and advection-dominated compressible Navier-Stokes equations.

## VI. LINEAR ELASTICITY BOUNDARY VALUE PROBLEMS

In solid and structural mechanics, linear elasticity mathematically describes the amount of deformation and stress a material undergoes due to prescribed loading conditions. The linear elastic boundary value problem are based on three tensor partial differential equations for the balance of linear momentum and six infinitesimal strain-displacement relations. The system of differential equations is completed by a set of linear algebraic constitutive relations. We solve for the deformation of a material undergoing loading by solving the equilibrium equation:

$$\begin{cases} -\nabla \cdot \boldsymbol{\sigma} = \mathbf{f}, & x \in \Omega \subset \mathbb{R}^3 \\ \mathbf{u} = 0, & x \in \Gamma_D \\ \boldsymbol{\sigma} \cdot \boldsymbol{\nu} = \mathbf{g}, & x \in \Gamma_N \end{cases} \quad (9)$$

where,

$$\boldsymbol{\sigma} = C\boldsymbol{\epsilon}, \quad \epsilon_{ij} = \frac{1}{2} \left[ \frac{\partial u_i}{\partial x_j} + \frac{\partial u_j}{\partial x_i} \right], \quad i, j = 1, 2, 3$$

$C$  is the governing material matrix,  $\mathbf{f}$  is the body force, and  $\mathbf{g}$  is the surface force. A material undergoes plane stress, provided the stress vector is zero in a specific plane. Our test problem will have zero stresses in the  $z$ -direction, hence,

$$\sigma_{3j} = \sigma_{i3} = 0, \quad \text{for } i, j = 1, 2, 3$$

In this paper, we solve the following linear elasticity boundary value plane stress problem on several spatial domains:

$$\begin{aligned} G \left[ \frac{\partial^2 u}{\partial x^2} + \frac{\partial^2 u}{\partial y^2} \right] + G \left( \frac{1+\nu}{1-\nu} \right) \left[ \frac{\partial^2 u}{\partial x^2} + \frac{\partial^2 v}{\partial y \partial x} \right] &= \sin(2\pi x) \sin(2\pi y) \\ G \left[ \frac{\partial^2 v}{\partial x^2} + \frac{\partial^2 v}{\partial y^2} \right] + G \left( \frac{1+\nu}{1-\nu} \right) \left[ \frac{\partial^2 v}{\partial y^2} + \frac{\partial^2 u}{\partial x \partial y} \right] &= \sin(\pi x) + \sin(2\pi y) \end{aligned} \quad (10)$$

where  $u_1 = u$  and  $u_2 = v$  are the deformation in the  $x$  and  $y$  direction respectively,  $G = \frac{E}{2(1+\nu)}$ ,  $E = 1$  GPa is the Young's modulus, and  $\nu = 0.3$  is the Poisson ratio of the material. We prescribe fixed boundary conditions. Hence, we imagine a plate that is fixed at the boundary, with periodic loading in the interior.

### A. W-PINNs

It is well established that PINNs have much difficulty resolving enforced boundary conditions (BC) [19]. The loss of the PDE is minimized at a much faster rate than the loss of the BC. Thus, PINNs neglects training the boundary, while emphasizes training in the interior. To rectify the error on the boundary, we enforce a severe penalty to the BC loss:

$$G(\theta) = \frac{1}{N_f} \left\| \nabla \cdot \tilde{\boldsymbol{\sigma}}(x, y, \theta) + \mathbf{f} \right\|_{\Omega}^2 + \frac{\omega_{BC}}{N_{BC}} \left\| \tilde{\mathbf{U}}(x, y, \theta) - \mathbf{U}(x, y) \right\|_{\partial\Omega}^2 = G_f(\theta) + \omega_{BC} G_{BC}(\theta) \quad (11)$$

where  $\omega_{BC} = 10,000$ . The choice of weights result in  $G_{BC}(\theta)$  to decrease at a faster than  $G_f(\theta)$  rate. This is similar to W-PINNs-DE, except domain extension is not needed since BCs are continuous, and loadings are smooth, periodic functions. Therefore, spurious oscillations are not generated during training. Below we present the W-PINNs algorithm to solve a plane stress linear elasticity boundary value problem (LEBVP).

---

#### Algorithm 2: W-PINNs ALGORITHM

---

- 1 Generate weights  $\theta \in \mathbb{R}^k$  and a deep neural network (DNN),  $\tilde{\mathbf{U}}(x, y, \theta)$ , where  $(x, y)$  are inputs to the network, and  $\tilde{\mathbf{U}} = [\tilde{u}, \tilde{v}]$  are the outputs. The number of layers, neurons per layer, and activation functions for each layer are prescribed by the user.
- 2 Sample points  $(x_n, y_n)$  from  $\Omega$  and  $w_n$  from  $\partial\Omega$ . Let  $N_f, N_{BC}$  correspond to the number of points sampled from the interior and boundary, respectively.
- 3 Generate  $G(\theta)$ :

$$G(\theta) = \frac{1}{N_f} \left\| \nabla \cdot \tilde{\boldsymbol{\sigma}}(x, y, \theta) + \mathbf{f} \right\|_{\Omega}^2 + \frac{\omega_{BC}}{N_{BC}} \left\| \tilde{\mathbf{U}}(x, y, \theta) - \mathbf{U}(x, y) \right\|_{\partial\Omega}^2$$

where  $\omega_{BC} = 10,000$

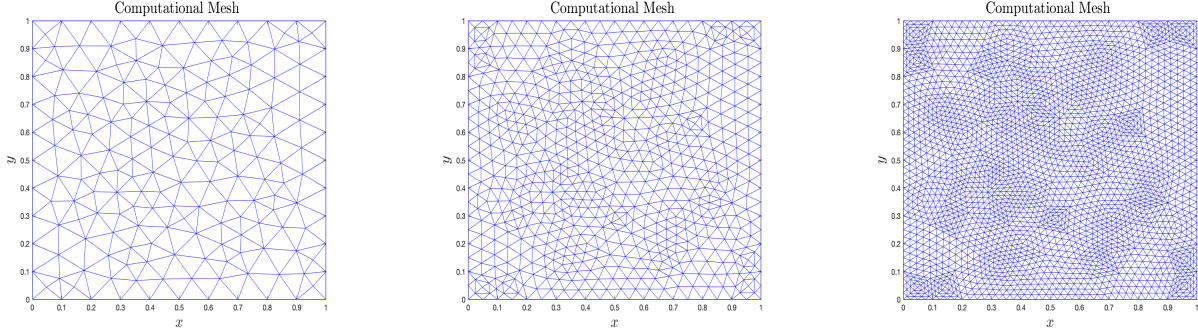
- 4 Update  $\theta$  by performing stochastic gradient descent, where  $\eta$  is the learning rate.: 
$$\theta = \theta - \eta \nabla_{\theta} G(\theta)$$
-

## VII. LINEAR ELASTICITY TEST PROBLEMS

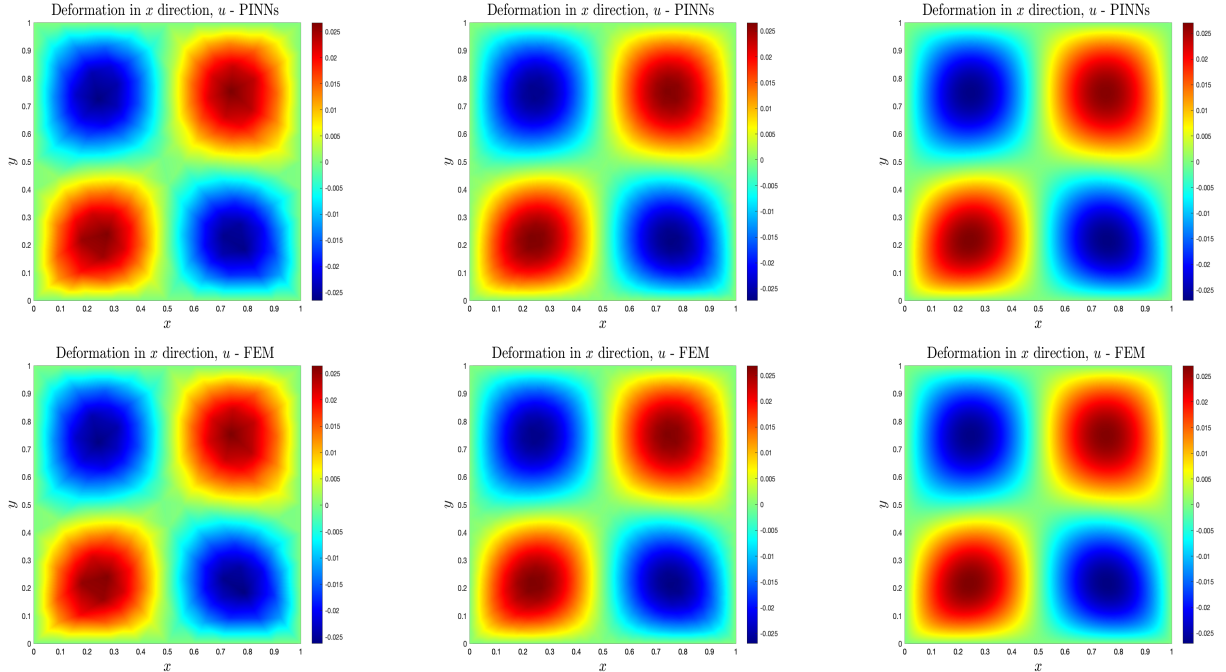
The finite element method (FEM) (Chen, 2013) is typically the method of choice to approximate solutions of LEBVP on a macroscale. It consists of discretizing the *weak* form of the PDE, and solving the discretized formulation on shape elements. We will compare the W-PINNs approximated solution of  $\mathbf{u} = [u, v]$  to an FEM approximation of the physical quantities. Each method is solved on several triangularized computational meshes. This study will investigate W-PINNs ability to solve LEBVP on four domains. In sections VII.A and VII.B, we show the effects of mesh refinement, in hopes of understanding W-PINNs convergence properties. We will measure the relative  $L_2$  error between the W-PINNs calculated solution, and a *ground-truth* FEM solution. Moreover, we plot the absolute errors to find regions which acquire the most error during training. In section VII.B, we will discuss the effects of over-refining the mesh and local mesh refinement. Sections VII.C and VII.D present results on two irregular domain, but detailed analysis is not provided. Similarly to the hydrodynamics study, each neural network has 7 layers with 30 neurons per layer, uses the  $\tanh(\cdot)$  activation function for non-linear layers, 199,350 epochs, and a learning rate of 0.0005. Lastly, we will use the entire mesh for training.

### A. Domain I

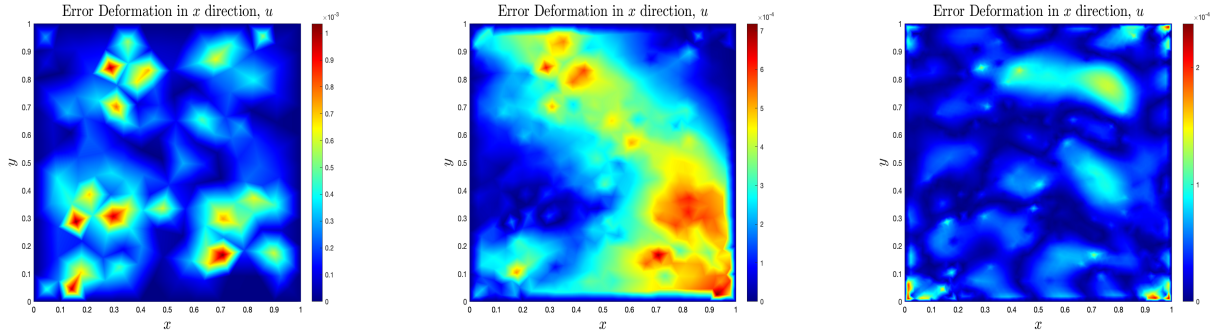
The first domain which we consider is a square domain, where  $(x, y) \in [0, 1]^2$ . In figure 14, we present three computational meshes for which W-PINNs and FEM are employed. In figures 15 and 17, we present the deformation in the  $x$  and  $y$  direction respectively on each computational mesh. As the mesh is further refined, we see the relative  $L_2$  error decreases significantly. Mesh III consists of  $N = 2,033$  mesh points, and achieves a relative  $L_2$  error of less than 0.2% for each physical quantity. However, in section VII.B, we will see the effects of over-refining the computational domain, and see that it increases the W-PINNs error.



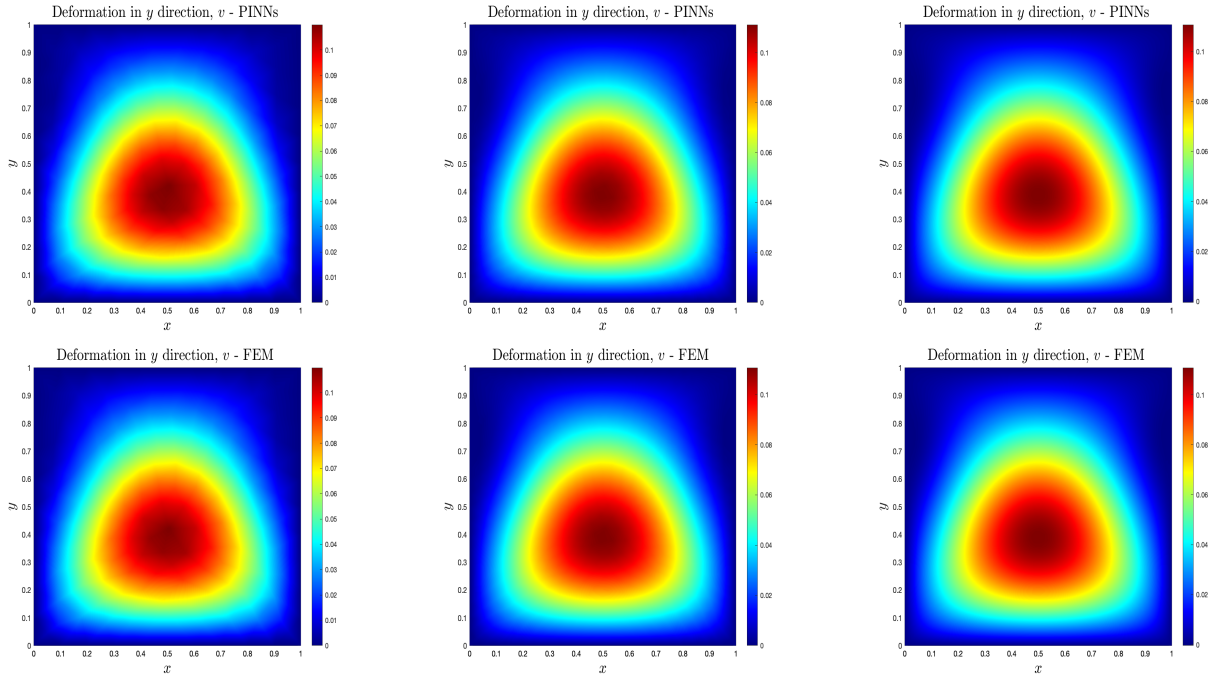
**Figure 14 – Computational Mesh I, II, and III**



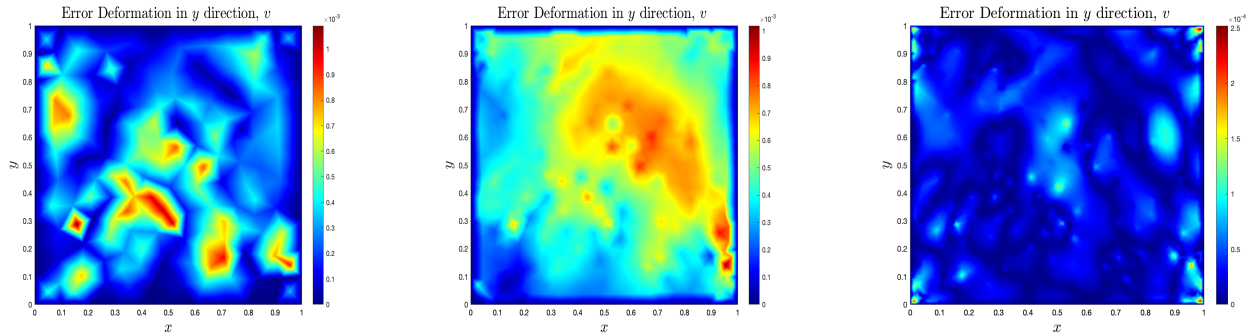
**Figure 15 – Deformation in  $x$  direction. Top: W-PINNs, Bottom: FEM, Left to Right: Mesh I, II, III**



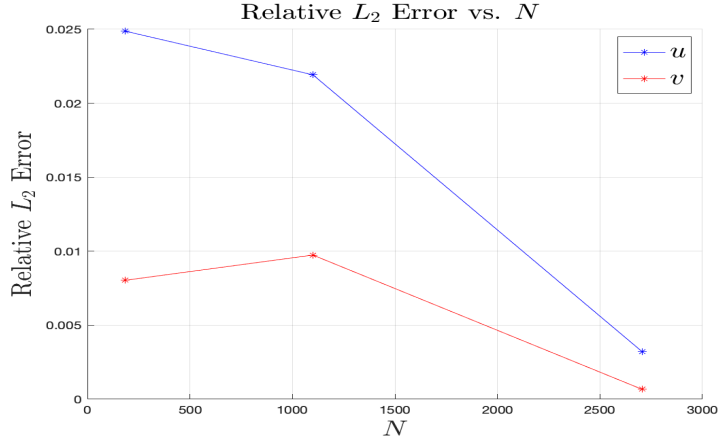
**Figure 16 – Absolute Error for deformation in  $x$  direction**



**Figure 17 – Deformation in  $y$  direction. Top: W-PINNs, Bottom: FEM, Left to Right: Mesh I, II, III**



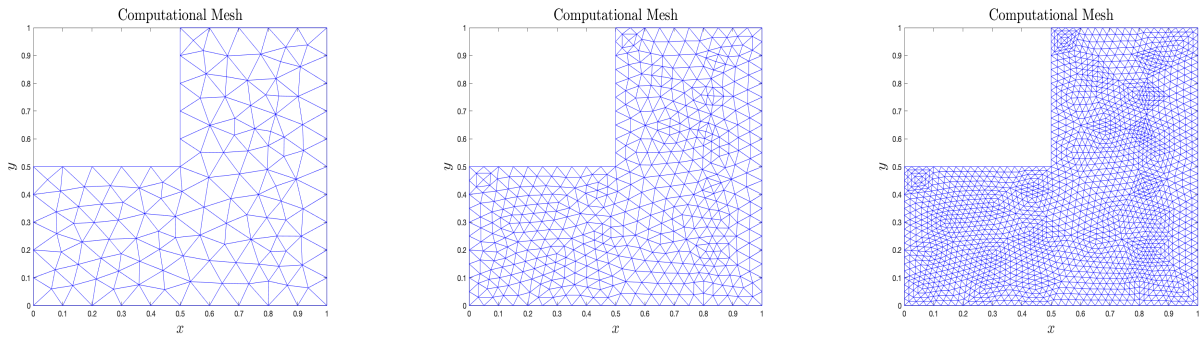
**Figure 18 – Absolute Error for deformation in  $x$  direction**



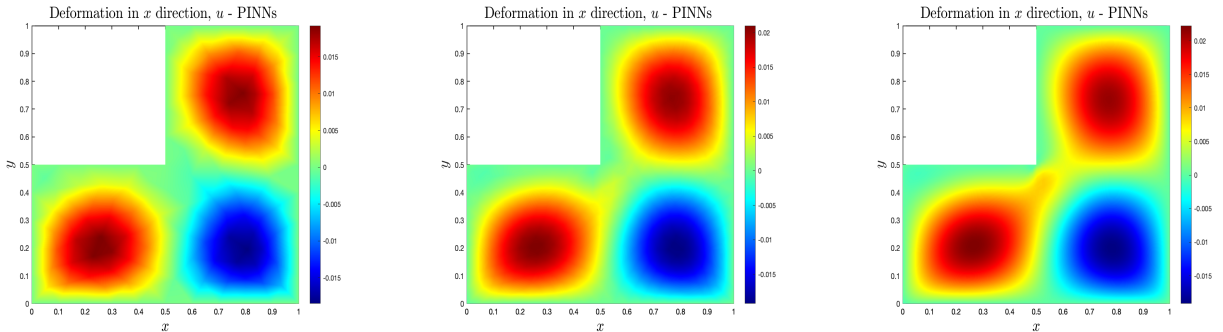
**Figure 19** – Relative  $L_2$  error versus number of mesh points,  $N$

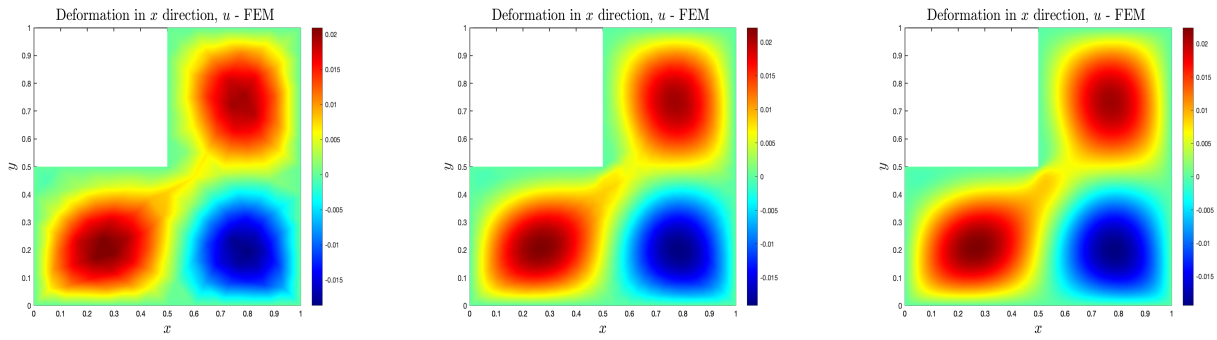
## B. Domain II

The second domain we consider is an L-shape domain. To further investigate the effects of mesh refinement on W-PINNs solutions, we perform a similar study as in section VII.A. In addition, we compare to a heavily refined ( $N = 7,986$ ) with a locally refined ( $N = 6,857$ ) computational mesh. Mesh VI ( $N = 2,033$ ) is chosen for this comparison since its corresponding relative  $L_2$  error is less than 1.5% for each physical quantity, as shown in figure 25. The locally refined mesh clusters points at the center corner,  $(x, y) = (0.5, 0.5)$ . Corners, such as at  $(x, y) = (0.5, 0.5)$  develop high numerical error since sharp domain changes are difficult for numerical methods to resolve. Local mesh refinement allows the FEM to capture solutions near these corners effectively. However, figure 27 demonstrates that W-PINNs performs better on Mesh VI than both the heavily refined and locally refined mesh. It is suspected that W-PINNs has a threshold to the number of points for which it may train on. Beyond this threshold, W-PINNs cannot minimize the  $G(\theta)$  sufficiently, hence the observed error accumulation in both refinement methods. Therefore, we suggest that  $N < 4,000$  is optimal for these class of problems. In future work, we wish to further investigate the effects of mesh refinement on W-PINNs.

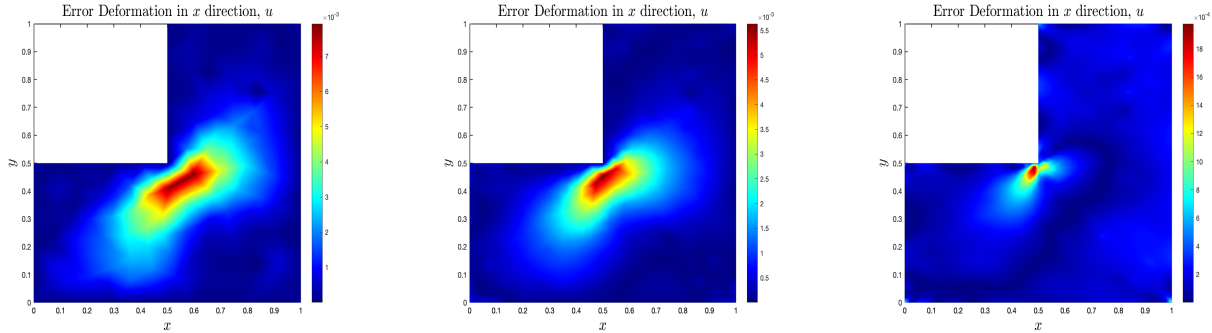


**Figure 20** – Computational Mesh IV, V, and VI

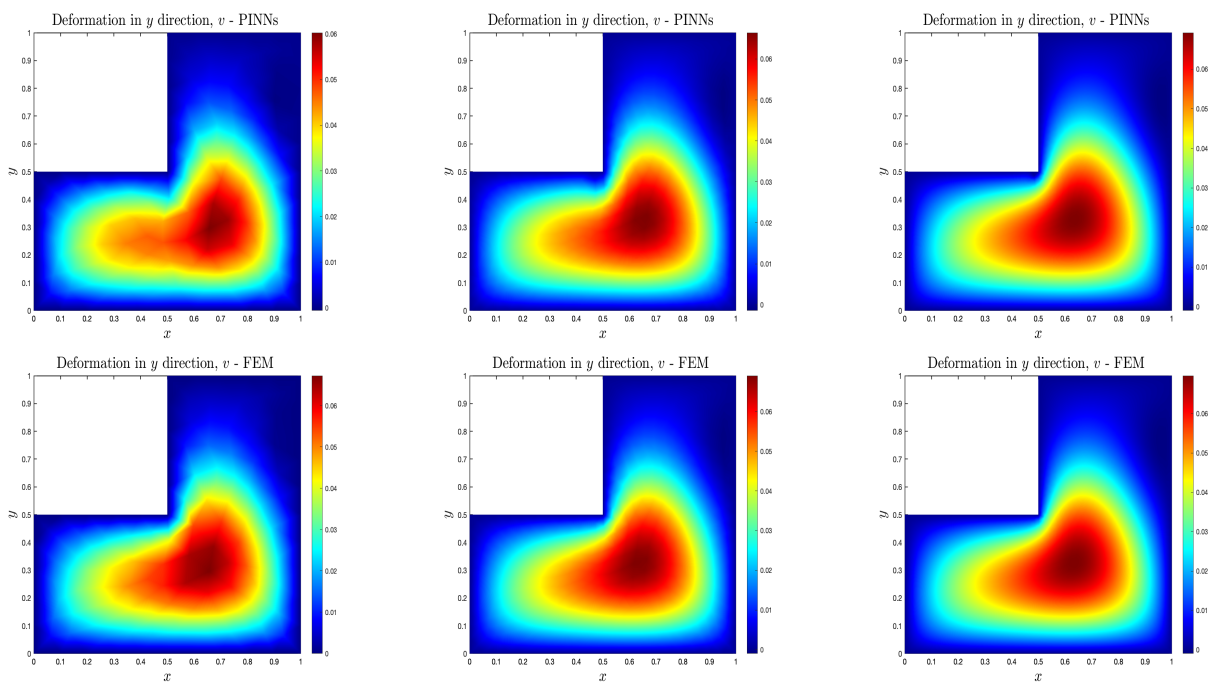




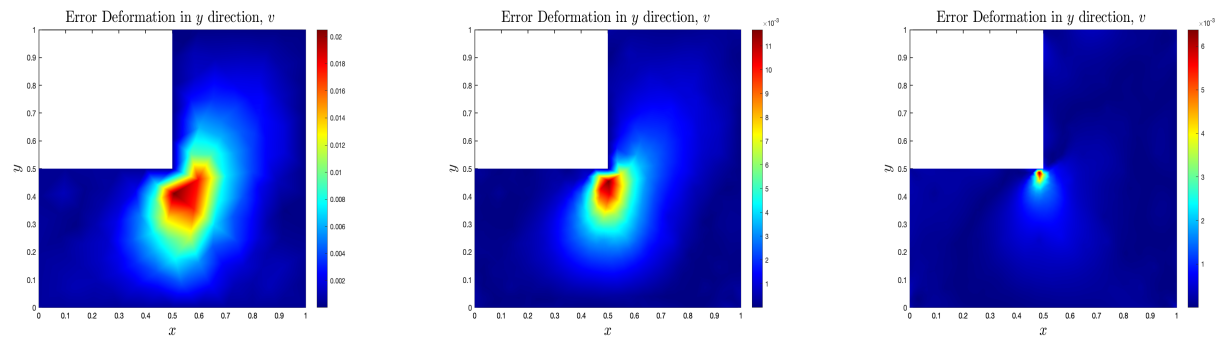
**Figure 21** – Top: W-PINNs , Bottom: FEM, Left to Right: Mesh IV, V, VI



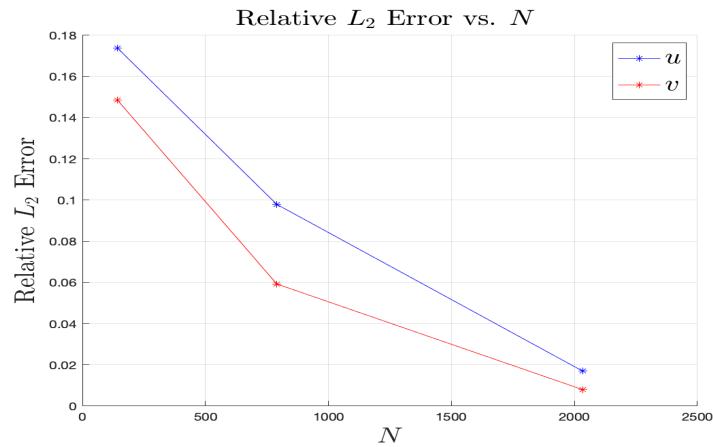
**Figure 22** – Absolute Error for deformation in  $x$  direction



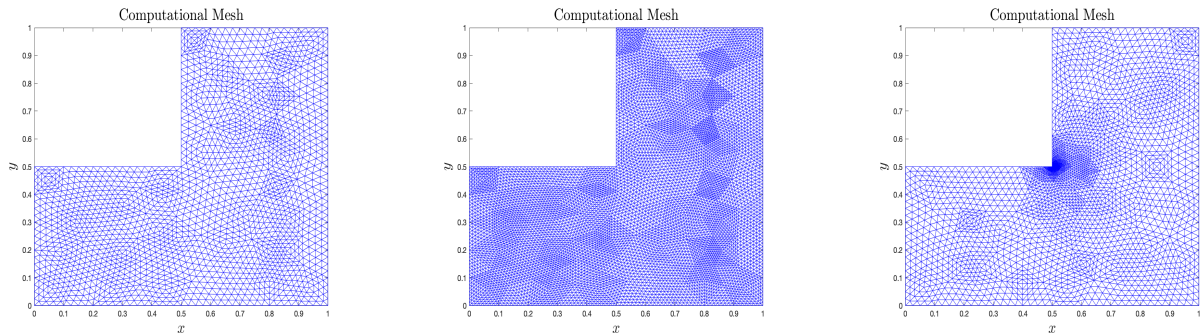
**Figure 23** – Top: W-PINNs , Bottom: FEM, Left to Right: Mesh IV, V, VI



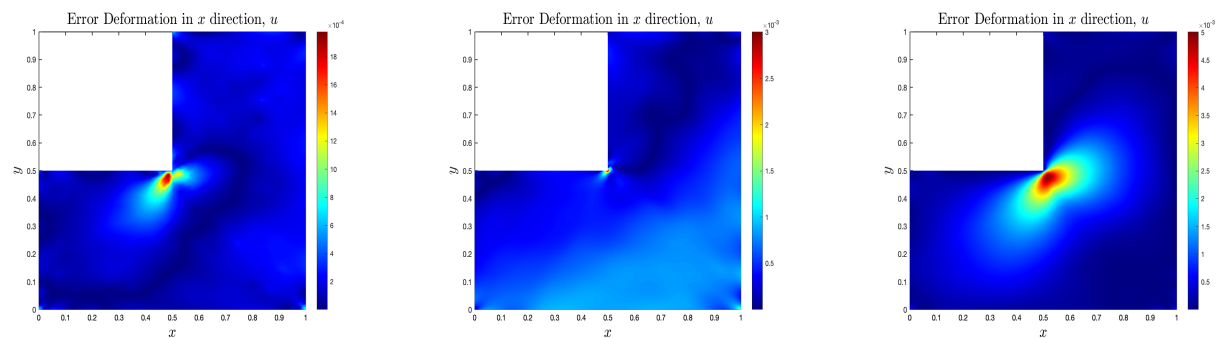
**Figure 24 – Absolute Error for deformation in  $y$  direction**



**Figure 25 – Relative  $L_2$  error versus number of mesh points,  $N$**



**Figure 26 – Left: Mesh VI, Middle: Refined Mesh, Right: Locally Refined Mesh**



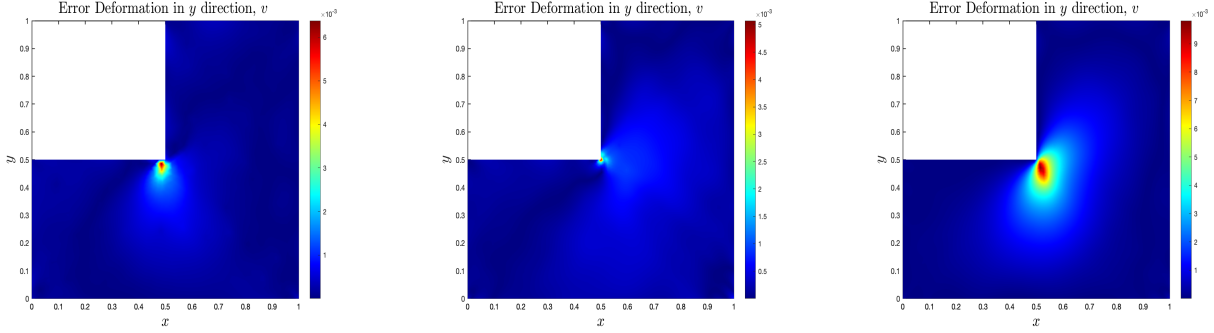


**Figure 27** – Top: Absolute error in deformation in  $x$  direction for each mesh. Bottom: Absolute error in deformation in  $y$  direction for each mesh. Left: Mesh VI, Middle: Refined Mesh, Right: Locally Refined Mesh

Domain	Mesh VI	Refined	Locally Refined
$\ u_{approx} - u_{exact}\ _2$	$1.4e - 02$	$4.9e - 02$	$7.8e - 02$
$\ u_{exact}\ _2$			
$\ v_{approx} - v_{exact}\ _2$	$9.0e - 03$	$2.0e - 02$	$4.8e - 02$
$\ v_{exact}\ _2$			

**Table XV** – Relative  $L_2$  errors

### Domain III

The third domain we consider is a square domain with a circular boundary of radius,  $r = 0.25$ , centered at  $(x, y) = (0, 0)$ . In section VII.A and VII.B, we've shown W-PINNs performs better when  $N < 4,000$ . Here, we discretize Domain III by employing 2,320 points, and solve on the triangulated domain. Figure 29 presents the deformation in the  $x$  and  $y$  direction, respectively, when solved on Mesh VII. The relative  $L_2$  errors are shown in Table XVI.

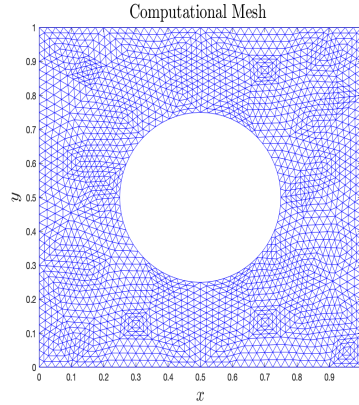


**Figure 28** – Mesh VII,  $N = 2,320$

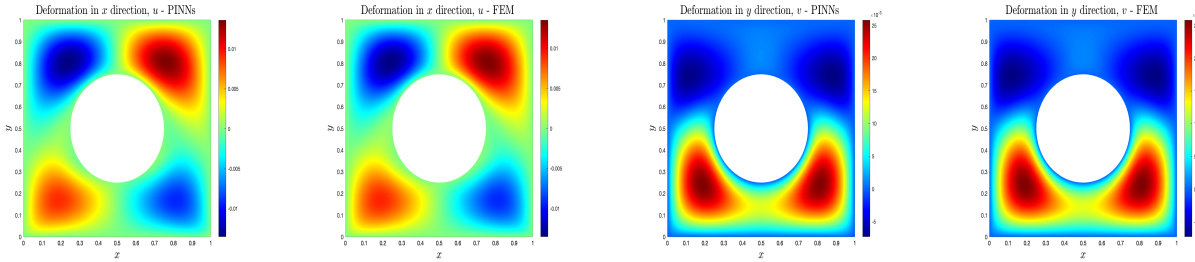


**Figure 29** – Deformation in  $x$  and  $y$  direction

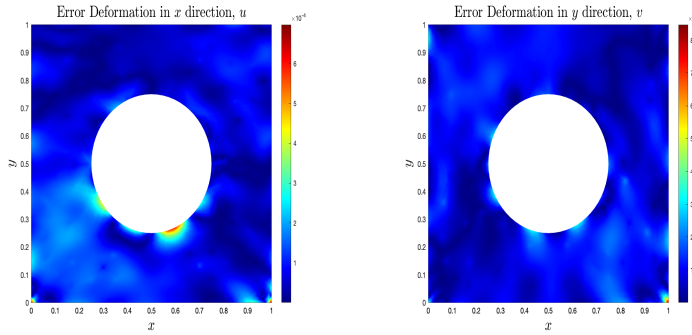


**Figure 30 – Absolute Error**

$\ u_{approx} - u_{exact}\ _2$	$\ v_{approx} - v_{exact}\ _2$
$\ u_{exact}\ _2$	$\ v_{exact}\ _2$
$9.9e - 03$	$9.8e - 03$

**Table XVI – Relative  $L_2$  errors**

### C. Domain IV

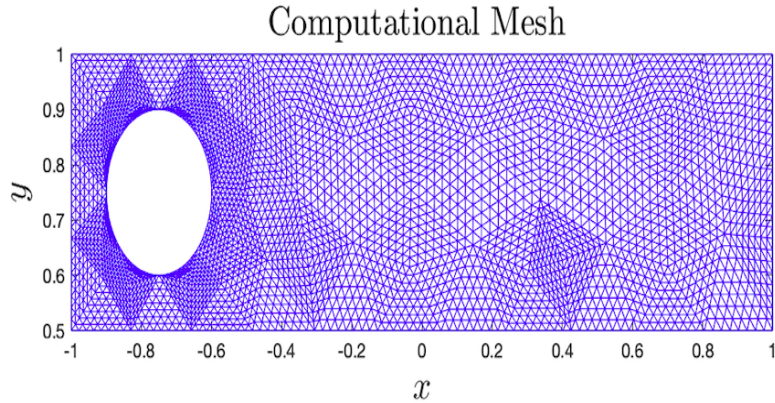


**Figure 31 – Mesh VIII,  $N = 3,600$**

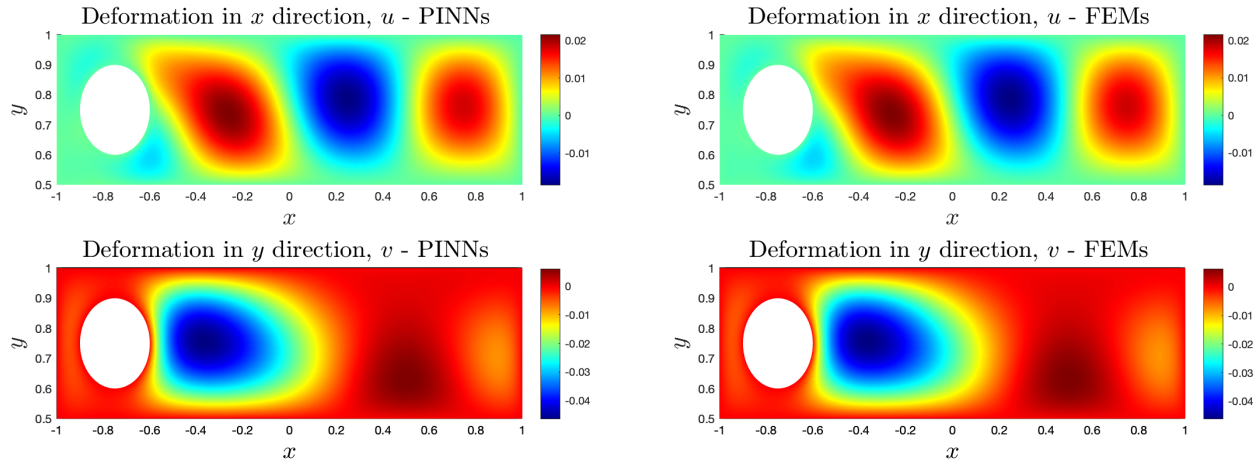


**Figure 32 – Deformation in  $x$  and  $y$  direction - Mesh VIII. Left: PINNs, Right: FEM**

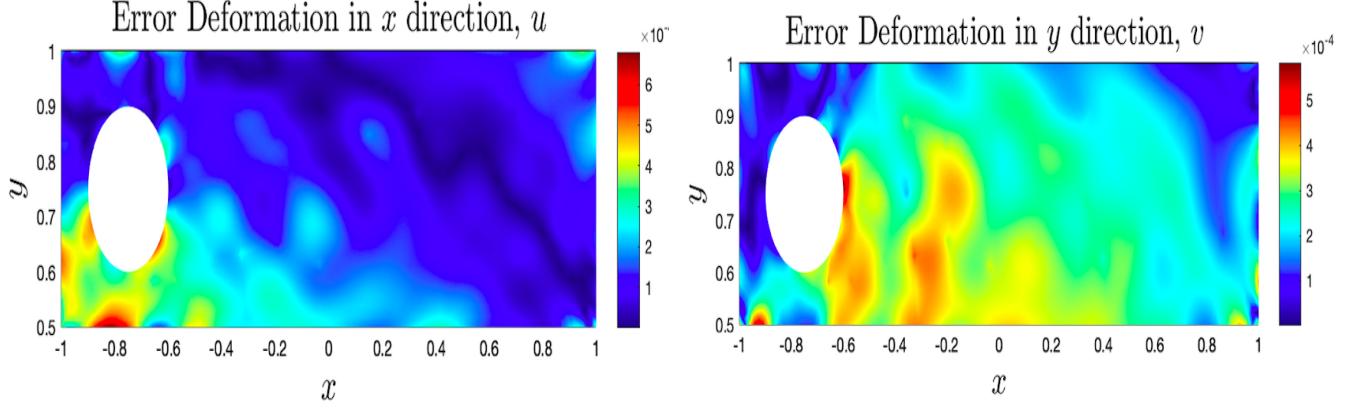


**Figure 33 – Absolute Error**

$\frac{\ u_{approx} - u_{exact}\ _2}{\ u_{exact}\ _2}$	$\frac{\ v_{approx} - v_{exact}\ _2}{\ v_{exact}\ _2}$
$3.6e - 03$	$2.5e - 03$

**Table XVII – Relative  $L_2$  errors**

## VIII. DISCUSSION II

In this study, we investigated W-PINNs ability to solve a LEBVP on a variety of domains and their corresponding computational meshes. The combination of a large penalty for  $G_{BC}(\theta)$  and a moderately refined grid, allows the neural network to accurately solve the BCs and the interior solution to the LEBVP. Although W-PINNs has proven to be more accurate than previous work [19], the FEM still outperformed the method. FEM solutions calculated solutions to the LEBVP in seconds, whereas some W-PINNs simulations took up to two hours. The W-PINNs framework presented in this paper is the first of which to achieve such accuracy using a PIDL framework. However, to truly be competitive with the FEM, it is necessary to further investigate parallelization and optimization techniques for W-PINNs.

In figures 19 and 25, the  $L_2$  relative error decays for each refinement. However, it was shown that over-refining and locally refining the mesh increases the error by as much as 6%, as shown in table XV. The error of the locally refined mesh was of great surprised, since (Mao et al., 2020) clustering points near regions susceptible to high error, while reduce the error. The locally mesh refinement presented in this paper is a form of clustering. Therefore, the fact that its solutions had the highest error in corner regions was peculiar.

## IX. FUTURE WORK

In future work, we aspire to extend W-PINN-DE into higher dimensions and simulate real-life problems, such as high energy release (denotation) problems. It is also essential to have a more robust theoretical background for this method than currently available. Therefore, it will be of great interest to further investigate and refine W-PINNs-DE mathematical formulation. This paper is merely the first reporting of the current research effort. In later work, we will present results for the isothermal Euler and Navier-Stokes equations solved using W-PINNs-DE. Moreover, we wish to investigate parallelization and optimization techniques for W-PINNs to make it more competitive to the FEM.

## X. REFERENCES

- [1] Roesner, K. G, Leutloff, D, Srivastava, R. C. (1995). *Computational fluid dynamics: Selected topics*. Berlin: Springer.
- [2] Chen, Y, Press, H. H. (2013). *Computational Solid Mechanics Structural Analysis and Algorithms*. Berlin: De Gruyter.
- [3] Thomas, J. W. (1999). *Numerical Partial Differential Equations: Conservation Laws and Elliptic Equations*. New York: Springer.

- [4] Golsorkhi, N. A, Tehrani, H. A. (2014). *Levenberg-marquardt Method For Solving The Inverse Heat Transfer Problems.* Journal of Mathematics and Computer Science, 13(04), 300-310. doi:10.22436/jmcs.013.04.03
- [5] Chen, Z. (2010). *Finite Element Methods and its Applications.* Berlin: Springer.
- [6] Mao, Z, Jagtap, A. D, Karniadakis, G. E. (2020). *Physics-informed neural networks for high-speed flows.* Computer Methods in Applied Mechanics and Engineering, 360, 112789. doi:10.1016/j.cma.2019.112789
- [7] Raissi, M, Perdikaris, P, Karniadakis, G. (2019). *Physics-informed neural networks: A deep learning framework for solving forward and inverse problems involving nonlinear partial differential equations.* Journal of Computational Physics, 378, 686-707. doi:10.1016/j.jcp.2018.10.045
- [8] Sirignano, J, Spiliopoulos, K. (2018). *DGM: A deep learning algorithm for solving partial differential equations.* Journal of Computational Physics, 375, 1339-1364. doi:10.1016/j.jcp.2018.08.029
- [9] Lu, L, Jagtap, A. D, Karniadakis, G. E. (2019). *DeepXDE: A Deep Learning Library for Solving Differential Equations.* ArXiv.org,arxiv.org/abs/1907.04502.
- [10] Cybenko, G. (1989). *Approximation by superpositions of a sigmoidal function.* Mathematics of Control, Signals, and Systems, 2(4), 303-314. doi:10.1007/bf02551274
- [11] Mishra, S, Molinaro, R. (2020). *Estimates on the generalization error of Physics Informed Neural Networks (PINNs) for approximating PDEs II: A class of inverse problems.* <https://arxiv.org/abs/2007.01138>
- [12] Pinkus, A. (1999). *Approximation theory of the MLP model in neural networks.* Acta Numerica, 8, 143-195. doi:10.1017/s0962492900002919
- [13] Sod, G. A. (1978). *A survey of several finite difference methods for systems of nonlinear hyperbolic conservation laws.* Journal of Computational Physics, 27(1), 1-31. doi:10.1016/0021-9991(78)90023-2
- [14] LeVeque, R. J. (2011). *Finite volume methods for hyperbolic problems.* Cambridge: Cambridge Univ. Press.
- [15] Michoski, C, Milosavljević, M, Oliver, T, Hatch, D. R. (2020). *Solving differential equations using deep neural networks.* Neurocomputing, 399, 193-212. doi:10.1016/j.neucom.2020.02.015
- [16] Patel, R. G, Manickam, I, Trask, N, Wood, M. A. (2020). *Thermodynamically consistent physics-informed neural networks for hyperbolic systems.* doi:<https://arxiv.org/abs/2012.05343>
- [17] Kim, J, Kim, A, Lee, S. *Artificial Neural Network-Based Automated Crack Detection and Analysis for the Inspection of Concrete Structures.* Applied Sciences, vol. 10, no. 22, 2020, p. 8105., doi:10.3390/app10228105.
- [18] Cazzanti, L, Khan, M, Cerrina, F. *Parameter Extraction with Neural Networks.* Metrology, Inspection, and Process Control for Microlithography XII, 1998, doi:10.1117/12.308780.
- [19] Wang, S, Tang, Y, Perdikaris, P. *Understanding and mitigating gradient pathologies in physics-informed neural networks.* 2020.

## APPENDIX A.

This appendix is dedicated to displaying the Mach number and total energy of each problem. The Mach number is the ratio between the flow velocity and the speed of sound, whereas the total energy is derived by the equations of state, which relates the pressure and energy of the fluid by:

$$M = \frac{u}{c}, \quad p = (\gamma - 1) \left[ \rho E - \frac{1}{2} \rho ||\mathbf{u}||^2 \right], \quad \mathbf{u} = u$$

where  $c = \sqrt{\gamma p / \rho}$ . The red dashed lines are the W-PINNs-DE approximation, and the blue line is the exact solution of the two quantities. In figures 34-39, we see that W-PINNs-DE satisfied the conservation of energy, verifying once more the accuracy of the method.

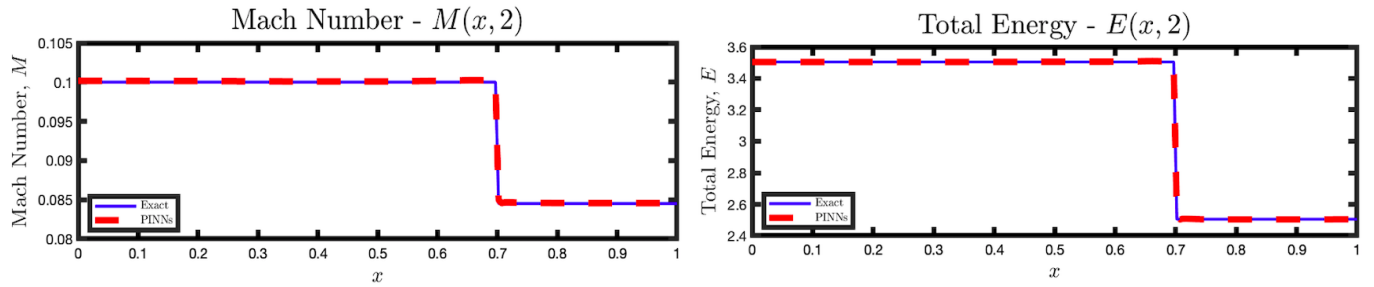


Figure 34 – Mach number and total energy at  $t = 2.0$  for the single contact discontinuity problem

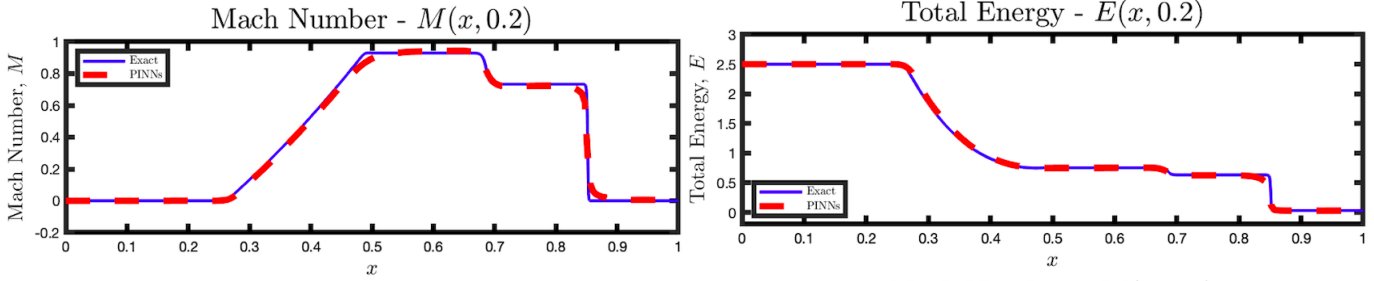


Figure 35 – Mach number and total energy at  $t = 0.2$  for the Sod shock-tube problem

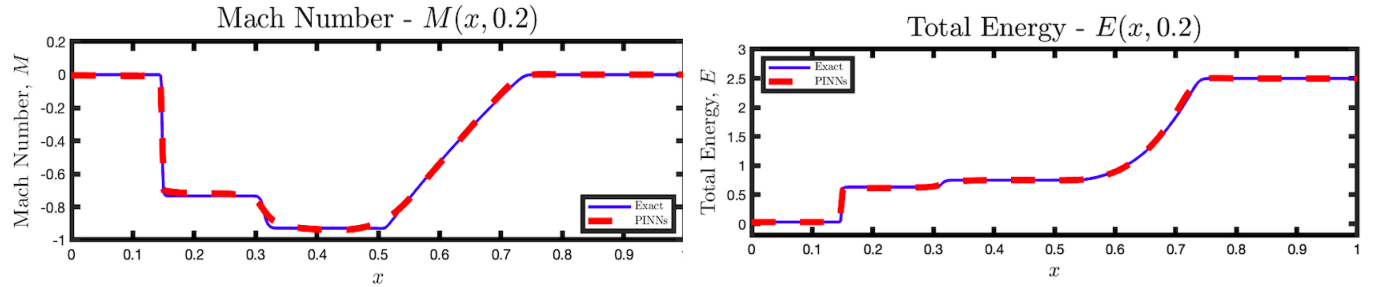


Figure 36 – Mach number and total energy at  $t = 0.2$  for the reverse Sod shock-tube problem

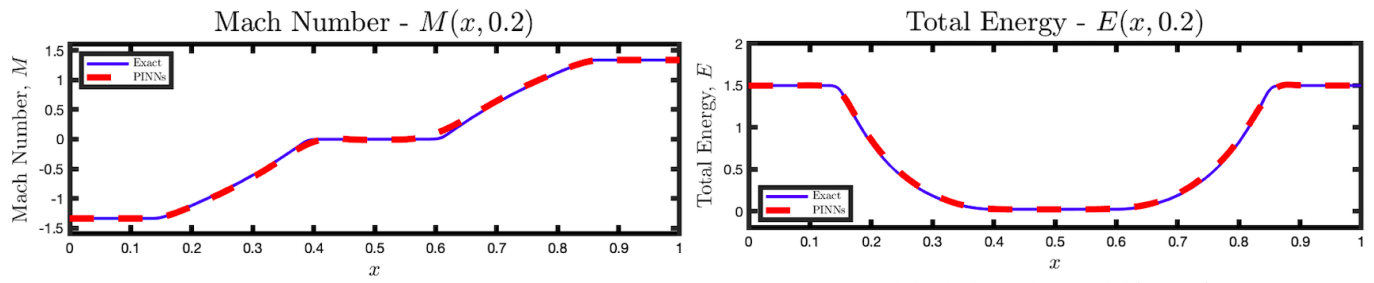


Figure 37 – Mach number and total energy at  $t = 0.2$  for the double expansion fan problem

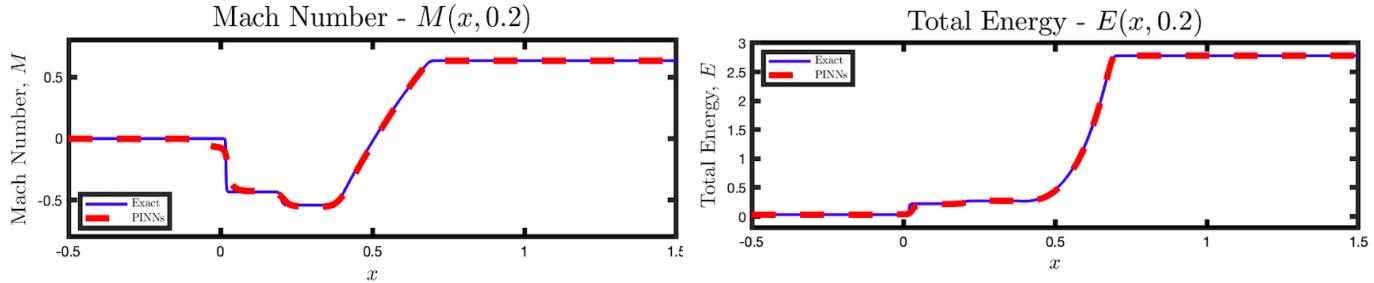
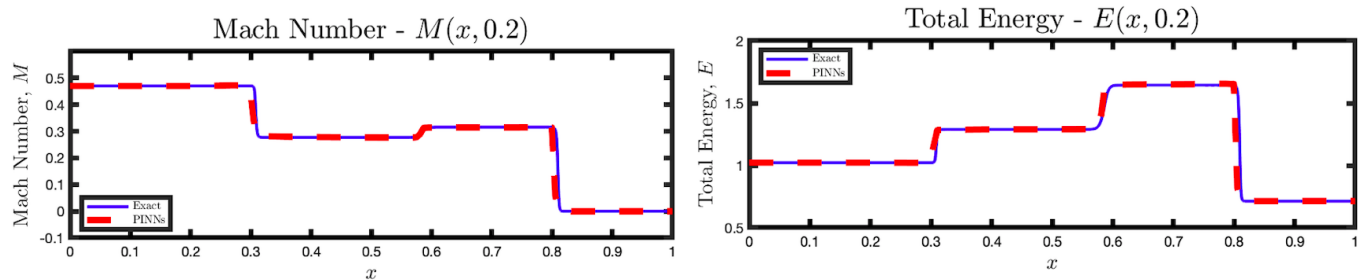
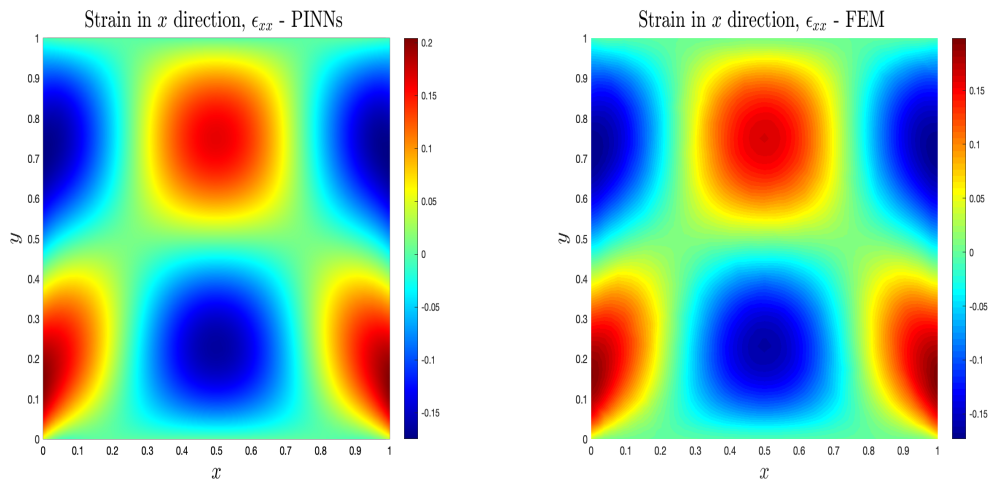


Figure 38 – Mach number and total energy at  $t = 0.2$  for the high-speed flow problem I



**Figure 39** – Mach number and total energy at  $t = 0.2$  for the high-speed flow problem II

## APPENDIX B.



**Figure 40** – Strain in  $x$  direction,  $\epsilon_{xx}$  - Mesh III

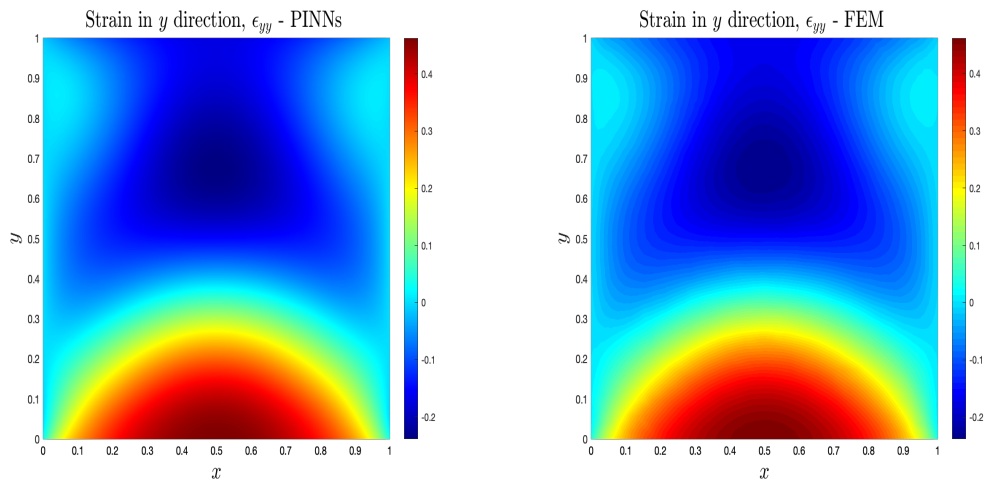


**Figure 41** – Strain in  $y$  direction,  $\epsilon_{yy}$  - Mesh III